PCCP

Robust band gaps in the graphene/oxide heterostructures– SnO/graphene/SnO

Journal:	*Physical Chemistry Chemical Physics*
Manuscript ID	CP-ART-03-2018-001483.R2
Article Type:	Paper
Date Submitted by the Author:	04-Jun-2018
Complete List of Authors:	Guo, Qing; Michigan Technological University, Physics Wang, Gaoxue; Michigan Technological University, Physics Pandey, Ravi; Michigan Technological University, Department of Physics Karna, Shashi; U.S. Army Research Laboratory

Robust band gaps in the graphene/oxide heterostructure– SnO/graphene/SnO

Qing Guo[#], Gaoxue Wang[#], Ravindra Pandey[#] and Shashi P. Karna[##]

[#]Department of Physics, Michigan Technological University, Houghton, Michigan 49931, USA
[##]Weapons and Materials Research Directorate, U.S. Army Research Laboratory, ATTN: RDRL-WM, Aberdeen Proving Ground,
Aberdeen, Maryland 21005-5069, United States

(June 4, 2018)

*Email: pandey@mtu.edu

Abstract

Graphene's applicability in nanoscale devices is somewhat limited because of the absence of a finite band gap. To overcome this limitation of zero band gap, we consider the vertically-stacked heterostructures consisted of graphene and SnO knowing that two-dimensional SnO films were synthesized recently. Calculations based on density functional theory find that the oxide monolayer can induce a noticeable band gap in graphene; the gap is 45 meV in graphene/SnO/graphene and 115 meV in SnO/graphene/SnO heterostructures. Additionally, graphene's band gap can be maintained under a relatively high electric field ($\approx 10^9$ V/m) applied to the heterostructures because of the electrostatic screening effect of the oxide layer. The calculated results suggest relative superiority of the graphene/oxide heterostructures over graphene/BN heterostructures for the nanoscale devices based on graphene.

1.0 Introduction

Graphene has attracted interest due to its remarkable electronic and mechanical properties [1-5], though the absence of a finite band gap has somewhat impeded graphene from practical applications. To overcome this limitation of zero band gap, several approaches including chemical doping [6, 7], mechanical strain [8-10], interlayer interaction with substrate [11, 12], and external electric field [13], have been employed to fabricate graphene-based nanoscale devices. Among these methods, fabrication of a van der Waals (vdW) heterostructure attracts particular attention. For example, opening of a small band gap at K was reported for the graphene/BN bilayer [14]. Other bilayer heterostructures, such as g-C_3N_4/graphene [15], MoS_2/graphene [16], and phosphorene/graphene [17], have also been used to induce the band gap in graphene. Compared to the bilayer heterostructures, the sandwiched trilayer structures have the advantage of not only inducing the band gap, but also providing the environmental stability to the graphene-based heterostructure. For example, a tunable band gap can be opened in the sandwiched BN/graphene/BN structure [18, 19] which could effectively reduce the environmental sensitivity of graphene in the graphene-based devices.

Recently, two-dimensional (2D) tin monoxide (SnO) films with intrinsic p-type semiconducting properties were synthesized [20-22]. A single phase SnO thin film which was fabricated on (001) yttria-stabilized zirconia substrate displayed superior performance in the p-channel thin film transistors [23]. SnO films with thickness of a few atomic layers were also fabricated on sapphire and SiO_2 substrates [24]. Recent experimental efforts include synthesis of the wafer-scale SnO monolayer from the interfacial oxide layers of metallic liquid tin [25]. On the theoretical front, first principles calculations reported the layer-dependence of the electronic properties of SnO films [26]. Calculations also demonstrated that 2D SnO films can be promising candidate for the photocatalytic water splitting [27] and sodium ion battery applications [28]. Our recent theoretical work predicted applicability of the bilayer

configuration composed of the SnO/graphene as field effect transistors (FETs). This is facilitated by a formation of the Schottky contact between the two layers which can tuned from p-type to n-type to Ohmic contact with an external electric field [29].

In this paper, we consider the vertically stacked heterostructures composed of graphene and the oxide monolayer to determine their stability and electronic properties. The considered heterostructures are tri-layers and are expected to be well-suited for device fabrication than the bilayer heterostructure. Our results based on density functional theory show that a band gap as large as 115 meV can be opened in graphene when it is sandwiched between SnO monolayers. Furthermore, we find the finite band gap to be robust under the external electric field up to $\approx 0.3 \times 10^{10}$ V/m. This robustness is found to be due to the electrostatic screening effect of the SnO layers as revealed in the charge density plots. Moreover, the predicted robustness is found to be relatively superior to that predicted for the graphene/BN heterostructure [30] under the applied electric field.

2.0 Computational method

Calculations were performed in the framework of the density functional theory (DFT). The generalized-gradient approximation (GGA) with Perdew-Burk-Ernzerhof (PBE) [31] exchange correlation functional together with Grimme's D2 method [32] representing the van der Waals interaction were employed as implemented in the Vienna ab-initio Simulation Package (VASP) program [33, 34]. We set the energy convergence to 10^{-7} eV and the kinetic energy cut-off to 520 eV. For the structural optimization, we use a grid of (5×3×1) k-points for sampling in reciprocal space. The criterion for force convergence was set to less than 0.01 eV/Å on each atom. For electronic properties calculations including total energy and density of states (DOS), we used a much denser k-points grid of (33×17×1). To eliminate the interaction between replicas due to periodic boundary conditions, a large vacuum layer more than 15 Å is built in the out-plane direction.

Calculations of the oxide/graphene heterostructures were performed in the context of the commensurate lattice approximation using graphene as a reference lattice. The periodic supercell was consisted of (1×3) cell for graphene and (1×2) cell for the SnO monolayer. The lattice mismatch between the oxide monolayer and graphene induced elongation (shortening) along x-(y-) direction in the oxide monolayer. A comparison of the results obtained using the (7×3) graphene/(8×2) SnO supercell and (1×3) graphene/(1×2) SnO supercell found the smaller supercell to reproduce very well structure and electronic properties of the bilayer heterostructure [29]. Note that the position of the Dirac point depends on how we choose the shape or size of the supercell for calculations. In our work, we have used rectangular 12-atom unit cell, and that there exists zero band gap for the freestanding graphene in this rectangular cell, thus confirming that the k-points grid is large enough to ensure the accuracy of calculations (Fig S2, Supplementary Information).

The calculated structural and electronic properties of the pristine SnO bulk [29] agree well with the previously reported experimental [24, 35] and theoretical results [22, 36-40] affirming the accuracy and reliability of the modeling elements employed in this study. It is to be noted that the heterostructures with a noticeable lattice mismatch have been predicted to have novel properties such as phosphorene/graphene [17] and WSe_2/graphene [41].

3.0 Results and discussions

3.1 Structural properties:

The geometrical configurations of the vertically-stacked heterostructures, namely SnO/graphene/SnO and graphene/SnO/graphene are shown in Fig. 1. Following the stacking nomenclature of graphite, the ABA-stacked configuration is composed of the AB-stacked bilayers displaying mirror symmetry relative to the central layer. The AAA-stacked configuration is composed of the AA-stacked bilayers on both side of the central layer. And the ABC-stacked configuration is composed of the AB-stacked bilayer on one side and the AA-stacked bilayer on the other side of the central layer. Initially, the registry index RI method [42] was employed to search the lowest energy

configurations for SnO/graphene bilayer as discussed in our previous work [29]. The results of the bilayer structures were then used to construct the trilayer configurations as shown in Figure 1. The total energy of the trilayer configuration was calculated with respect to displacement of the graphene layer. The ABA-stacked trilayer is found to be the energetically preferred configuration as displayed in Figure S2 (Supplementary Information).

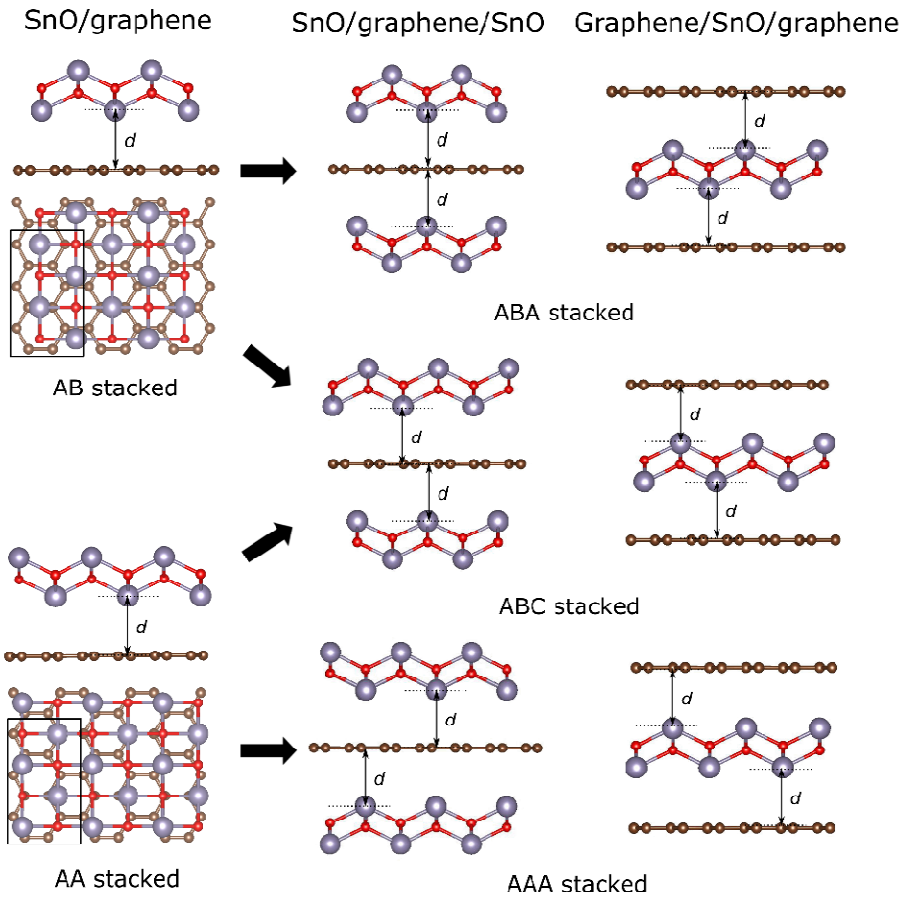

Figure 1. The stacking configurations of SnO/graphene heterostructures considered. Color code: C: small brown sphere, Sn: large grey sphere and O: small red sphere.

Table 1 lists the calculated structural properties and the band gap of SnO/graphene heterostructures. Not surprisingly, the ABA-stacked configuration is more energetically stable for the SnO/graphene/SnO and graphene/SnO/graphene heterostructures. In the ABA-stacked configuration with the mirror symmetry, the

interlayer distances are very similar: ≈3.46 Å for SnO/graphene/SnO and ≈3.42 Å for graphene/SnO/graphene. In the AAA-stacked configuration, the interlayer distance is ≈3.48 Å, very close to the interlayer distance of 3.47 Å calculated for the AA-stacked bilayer [23]. While in the ABC stacked mode, the interlayer space is 3.42 Å on the 'AB-stacked' side and 3.45 Å on the 'BC-stacked' side. This is similar to what has been calculated for the constituent bilayers: 3.42 Å for AB-stacked and 3.47 Å for the AA-stacked bilayers. The intralayer bond distances, R_{Sn-O} and $R_{C-C,}$ are calculated to be 2.35 (2.24) Å and 1.42 (1.41) Å in x- (y-) direction, respectively. Note that bulk SnO has a tetragonal PbO layered structure with the interlayer distance of 2.48 Å [23].

The DFT results show that the heterostructures follow the trend in stability as predicted for the bilayers [23] with ABA-stacked heterostructure being energetically preferred. Additionally, the binding energy of a heterostructure is slightly higher than the sum of binding energies of the constituent bilayers suggesting that the stable oxide/graphene heterostructures can be fabricated. A comparison of SnO/graphene/SnO and graphene/SnO/graphene heterostructures within the same stacking mode finds the latter heterostructure to have a smaller binding energy. This is due to the fact that the SnO monolayer owns a certain thickness which enlarges the distance between two graphene layers thus reducing contributions from the interlayer interactions. For example, the calculated distance between two graphene layers in ABA-stacked graphene/SnO/graphene is 9.1 Å while distance between the oxide layers in ABA-stacked SnO/graphene/SnO is 6.9 Å.

Table 1. Calculated binding energy ($E_{binding}$), interlayer spacing ($d_{interlayer}$) and band gap (E_{gap}) of SnO/graphene heterostructures.

Heterostructure	Stacking configuration	$E_{binding}$ / unit cell (eV)	$d_{interlayer}$ (Å)	E_{gap} (meV)
SnO/graphene	AB	0.484	3.42	8
SnO/graphene	AA	0.460	3.47	-
SnO/graphene/SnO	ABA	0.993	3.46, 3.45	115
SnO/graphene/SnO	ABC	0.987	3.42, 3.45	34
SnO/graphene/SnO	AAA	0.955	3.48, 3.47	58
graphene/SnO/graphene	ABA	0.969	3.42, 3.43	45
graphene/SnO/graphene	ABC	0.983	3.42, 3.45	7
graphene/SnO/graphene	AAA	0.925	3.48, 3.47	68

3.2 Electronic properties

To simulate SnO/graphene/SnO trilayer, we have employed rectangular unit cell containing 12 carbon atoms for which the high-symmetric points are indicated by X, Y and S points in the first Brillouin zone (BZ) (Fig S2, Supplementary Information). In this k-point setup, the band structure of free-standing graphene (Fig. 2(a)) is displayed showing that the Dirac point of free-standing graphene is located at the Γ for the rectangular 12-atom unit cell. Figs. 2(b), 2(c) and 2(d) displays the band structures of the energetically preferred configurations of the SnO/graphene/SnO and graphene/SnO/. The high symmetry points in the first BZ of the rectangular supercell are shown in the inset of Fig 2(a).

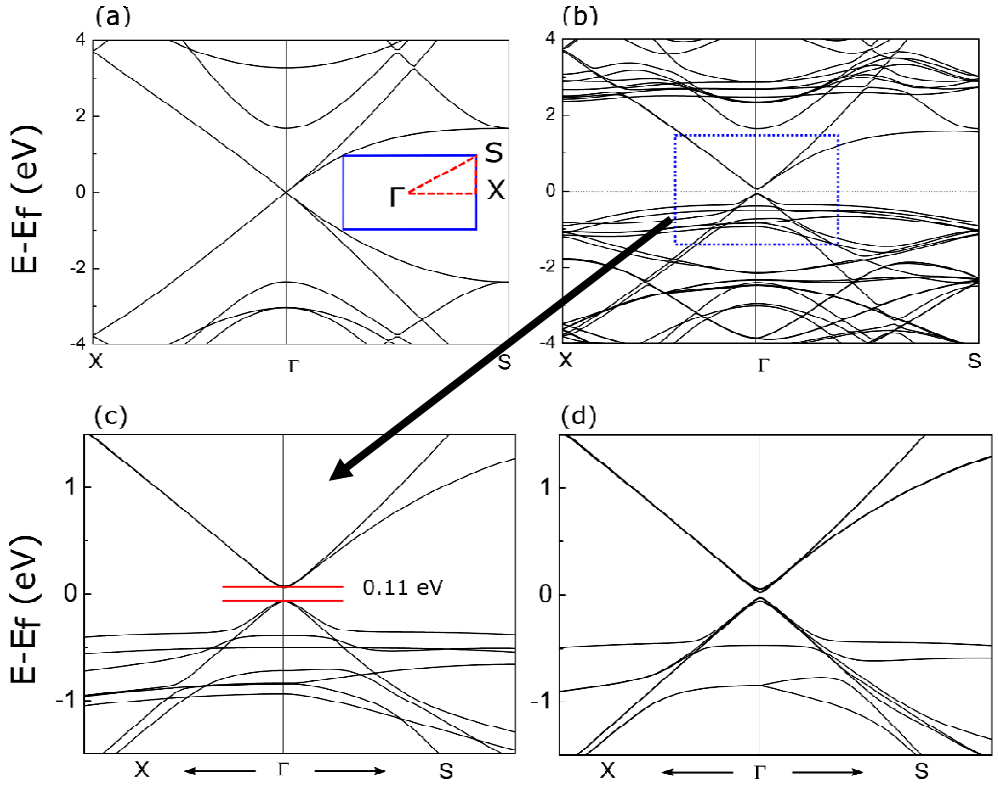

Figure 2. Calculated band structures of (a) free-standing graphene and (b) ABA stacking SnO/graphene/SnO heterostructure (c) zoom-in band structures around Γ indicated by the blue dash line box in 2 (b), and (d) graphene/SnO/graphene heterostructure.

In the ABA-stacked SnO/graphene/SnO heterostructure, a noticeable finite band gap of 115 meV is opened up in graphene which is about two times of that predicted for the ABA-stacked BN/graphene/BN heterostructure [30]. Note that calculations using the hybrid functional HSE06 yieldthe band gap to be 240 meV. Such a large gap opening is mainly due to interaction between the oxide layers and graphene which breaks the equivalence in carbon sublattice of graphene. This unequal interaction is clearly illustrated by the partial charge density plots displayed in Fig. 3 (a).

In Fig. 3 (a), the partial charge density is plotted in the energy range from -1 eV to 0 eV (i.e. Fermi energy) and the isosurface in the 3D plot is 0.02 e/Å ^{3}. Slice 1, 2, 3 are the 2D views sliced at the positions of different carbon atoms indicated in the 3D partial charge density plot. From 2D view of the slices, we can clearly see that C

atoms which are beneath Sn atoms (slice 1) interact more strongly than the other C atoms (slice 2, 3), and the interaction is enhanced by the presence of the mirror-symmetric oxide layer. Likewise, the charge density difference plots shown in Fig. S3 (Supplementary Information) confirm the presence of interaction between graphene and the oxide monolayer.

In contrast, a loss of mirror-symmetric layer for the ABC-stacked heterostructure leads to a smaller degree of interaction yielding the gap opening of ≈34 meV. This is also the case with the graphene/SnO/graphene heterostructure for which absence of a mirror-symmetric layer in the ABC-stacked configuration leads to a smaller degree of C-Sn atomic interaction yielding a negligible gap opening of ≈7 meV (Table 1).

The extent of the interlayer interaction in the heterostructures can also be seen in the electron localization function (ELF) plots given in Fig. 3 (b). For the ABA-stacked SnO/graphene/SnO heterostructure, deformation of the Sn atom's lone pair sphere facing C atom is mainly due to a higher degree of the interlayer interaction in the heterostructure. Note that the ELF sphere is associated with the lone pair formed by Sn ($5p_z$) and Sn (5s)-O($2p_z$) orbitals at the oxide monolayer surface [22].

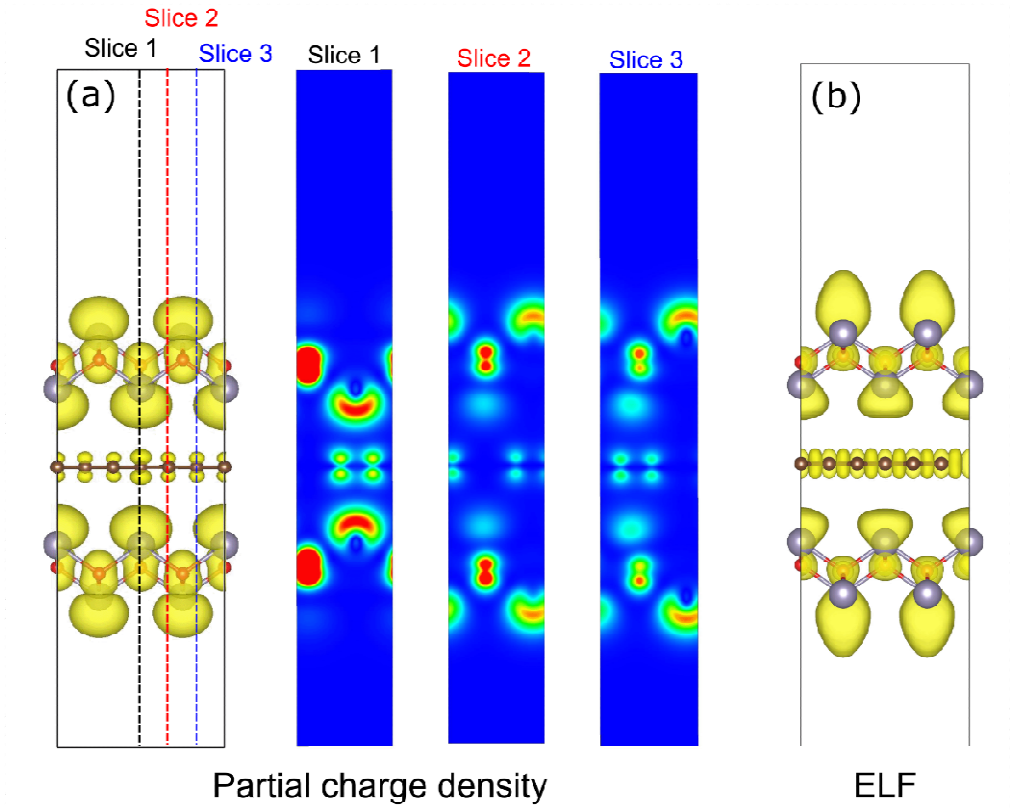

Figure 3. ABA-stacked SnO/graphene/SnO heterostructure: (a) the partial charge density plots in the energy range from -1 eV to 0 (i.e. Fermi energy) with the iso-surface of 0.02 e/Å ^{3}. 2D slices indicated by the black, red and blue lines are also plotted. (b) ELF with the isosurface value of 0.8.

To determine the sensitivity of our results on the functional forms describing vdW interactions, we perform a limited set of calculations using optB88-vdW functional form [43-46]. The results show that stability and opening of the band gap do not sensitively depend on the way we describe vdW interactions in these trilayer configurations (Tables. S1 and S2, Supplementary Information).

3.3 Effect of the tensile/compressive strain applied to heterostructures.

To affirm the fact that the interaction between the oxide monolayer and graphene in the heterostructure is the cause of opening of the graphene's band gap, additional calculations were performed on the heterostructures applying the perpendicular strain ranging from -10% to +10%. The results are shown in Fig. 4 (a). Interestingly, the

graphene's band gap increases to 140 meV for the compressive strain of 8% (i.e. $d_{interlayer}$=3.16 Å). On the other hand, application of the perpendicular tensile strain of about 9% (i.e. $d_{interlayer}$=3.78 Å) yields the band gap of 74 meV suggesting the reduced degree of interaction between the oxide monolayer and graphene.

The orbital projected band structures shown in Fig. 4 (b)~(d) for the case of the perpendicular compressive strain of 8% find lifting of degeneracy in the conduction levels of graphene. The lone pair at the SnO monolayer surface formed by Sn ($5p_z$) and Sn (5s)-O($2p_z$) orbitals [22] overlaps with C ($2p_z$) orbitals and induces a strong interaction between the two layers in the heterostructure.

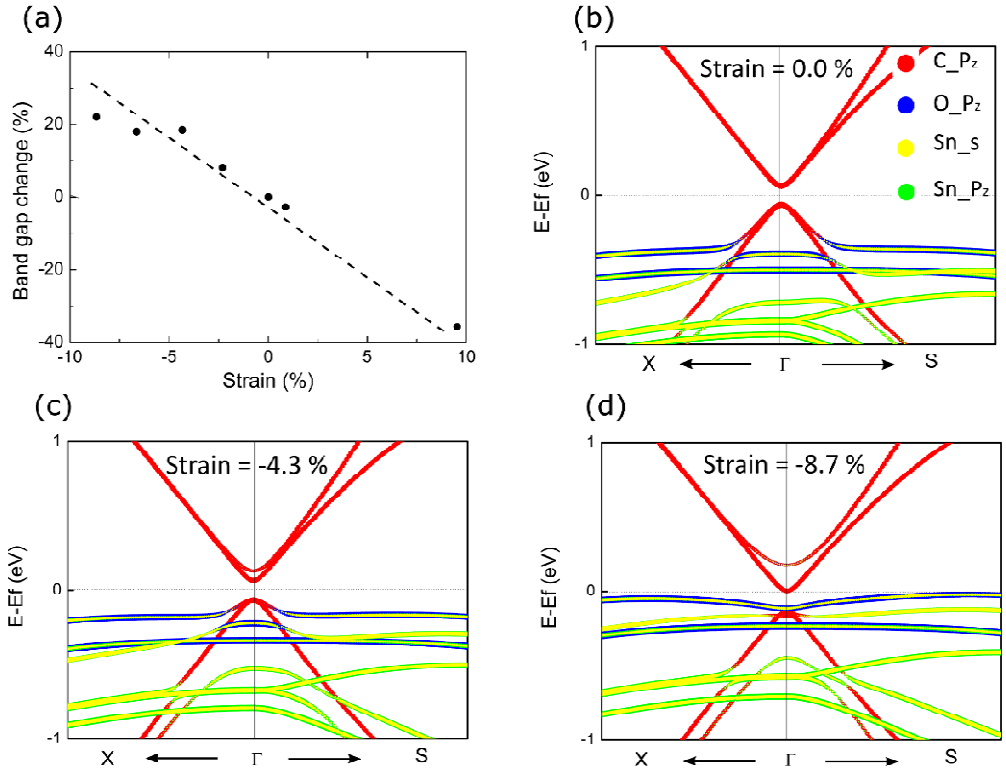

Figure 4. ABA-stacked SnO/graphene/SnO heterostructure: (a) calculated band gap of graphene as a function of strain applied perpendicular to the heterostructure. (b), (c) and (d) the projected band structures around Γ associated with the perpendicular strain of 0%, -4.3% and -8.7%. In (b), (c) and (d), the red, blue, yellow and green lines show the orbital projected C_p_z, O_p_z, Sn_s and Sn_p_z bands, respectively

3.3 Effect of the external electric field on the heterostructures

The electric field is applied vertically along the stacked direction of the

heterostructure. Fig. 5 (a) displays variation in the band gap with the applied electric field for the ABA-stacked heterostructures. Remarkably, the band gap is found to be independent of the electric field up to 3×10^9 V/m for SnO/graphene/SnO heterostructure. It should be pointed out that the electric field at the order of ~10^9 V/m is within the range of the fabricated devices. In contrast, although a band gap is induced in graphene trilayer by applying electric field, it is not stable; the band gap opens up to its maxima at the electric field of 0.5×10^9 V/m and then begins to close with the increase in the electric field [47, 48]. A similar results has also been seen for the graphene/BN/graphene heterostructure where opening of the band gap of graphene is only 57 meV for the electric field of 1×10^9 V/m [30].

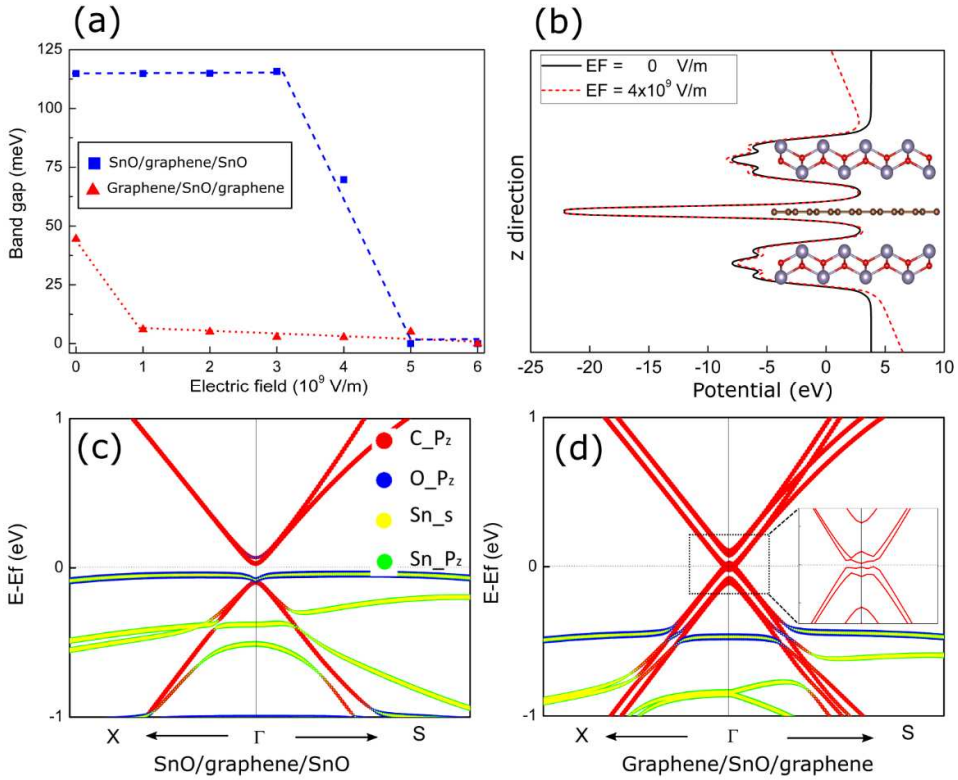

Figure 5: ABA-stacked SnO/graphene heterostructures: (a) calculated band gap as a function of the applied electric field. (b) Planar average electrostatic potential along the z-direction. Color code: Black line, EF=0 and red dot line. EF=4×10^9 V/m. (c) Projected band structure around Γ point at EF=4×10^9 V/m for SnO/graphene/SnO. (d) Projected band structure around Γ point at EF= 1×10^9 V/m for graphene/SnO/graphene. In (c) and (d), the red, blue, yellow and green lines stand for the orbital projected C_p_z, O_p_z, Sn_s and Sn_p_z bands, respectively

Our calculations find that the band gap of SnO/graphene/SnO heterostructure is solely derived from graphene. Application of an external electric field from bottom to top leads to increase of the VBM edge of top SnO layer, while decreasing that of the bottom SnO layer. The middle graphene layer appears to be relatively unaffected. However, when the electric field becomes larger than 3×10^9 V/m, the VBM of top SnO layer is higher than that of graphene's, yielding the gap to be between the VBM of top SnO layer and the CBM of graphene layer (Fig. 5 (c)). Increasing the electric field then induces a linear-like deduction of the heterostructure's band gap due to the stark effect till the band gap closes for the electric field of $\sim5\times10^9$ V/m.

To further understand this robustness of the band gap under such a high electric field, the planar average electrostatic potential is plotted in Fig. 5 (b). We find that a wide barrier of the outer oxide layers is essentially shield graphene. This is not the case with the graphene/SnO/graphene heterostructure for which the outer graphene layers are directly exposed to the external electric field thereby closing the gap. The Dirac point of graphene on the higher potential side goes below Fermi level while the Dirac point of the other graphene layer goes above Fermi level as shown in Fig. 5 (d) and overlap of Dirac cones yields nearly zero band gap under the external electric field.

Additional calculations have been carried out to illustrate the influence of SnO substrate's thickness on the electronic properties of the heterostructure. For the ABAA-stacked structure consisted of SnO monolayer/ graphene/SnO bilayer and ABAAA- stacked structure consisted of SnO monolayer/ graphene/ SnO trilayer, the results show that top of the valence band associated with SnO layers have risen to the Fermi level with the increase in the substrate thickness. Consequently, the band gap is closed in graphene/oxide heterostructures with a thicker SnO substrate which will result in an Ohmic conductivity of the device (Fig S4, Supplementary Information)

3.4 Electronic transport properties

Next, we calculate the I-V characteristics of the SnO/graphene heterostructure using the scanning tunneling microscope (STM) setup [29]. The tunneling current

from the sample to the tip at location $\vec{r}_t$ is obtained using the Tersoff and Hamann approximation [49] :

$$I(\vec{r}_t;V) \approx \frac{2\pi e}{\hbar}\int_{-\infty}^{+\infty} \rho_t\left(E-\frac{eV}{2}\right)\rho_s\left(\vec{r}_t;E+\frac{eV}{2}\right)F(E)dE \qquad (1).$$

Here, ρ_t and ρ_s are the electron density of the tip and the sample beneath the tip. $F(E)$ is the term including the effect of thermally excited electrons as proposed by He *et al*. [50]. In calculations, a finite Au_{13} cluster with the icosahedral shape was used to simulate the tip. The tunneling current is essentially an integration of the convolution of density of states (DOS) of the tip and sample, and will depend on the valence and conduction states near the Fermi level of a given heterostructure.

Fig. 6 (a) displays a comparison of the I-V characteristics of the SnO/graphene heterostructures. The inset is the zoomed figure in the red rectangular box showing that the graphene/SnO/graphene heterostructure behaves like a good conductor. This is caused by the nearly zero band gap of graphene, thus the electron tunneling between the tip and the top graphene layer occurs at a very small bias field. While for the other two heterostructures (i.e. SnO/graphene and SnO/graphene/SnO), since the electron tunnels between the tip and the top SnO layer, the I-V characteristics show diode-like characteristics due to the band gap of the SnO monolayer. We also notice that the breakdown voltage of SnO/graphene/SnO is lower than that of the SnO/graphene bilayer. This is due to fact that the Schottky barrier of the trilayer is about 0.1 eV lower relative to that in the bilayer.

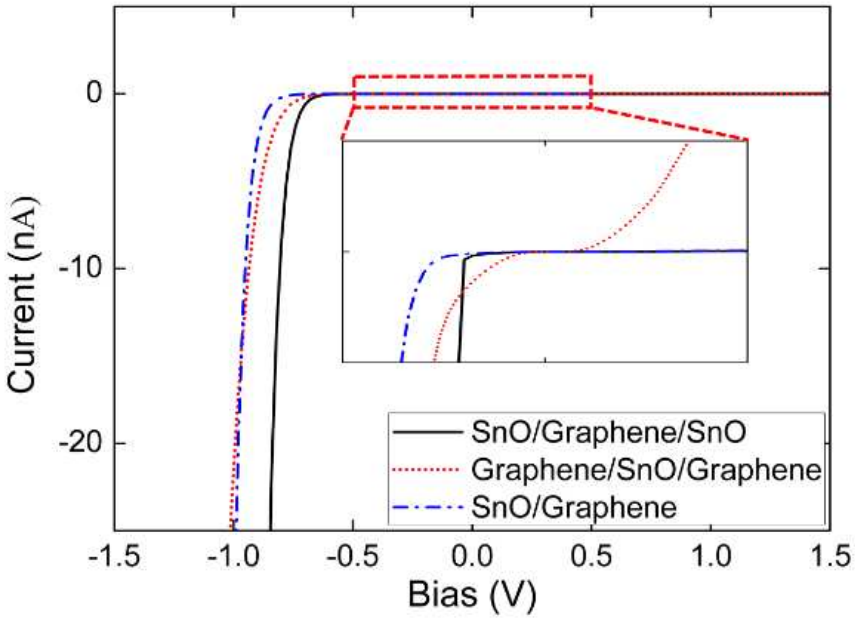

Figure 6: Calculated I-V characteristics of SnO/graphene heterostructures.

The topology of the heterostructures can be characterized by the simulated STM images and (14×18) $Å^2$ images of SnO/graphene heterostructures are displayed in Fig. 7 obtained in the constant height mode with the tip distance of 3 Å. For SnO/graphene/SnO, the top Sn atoms are associated with the bright regions whereas the top carbon rings in graphene/SnO/graphene are clearly seen.

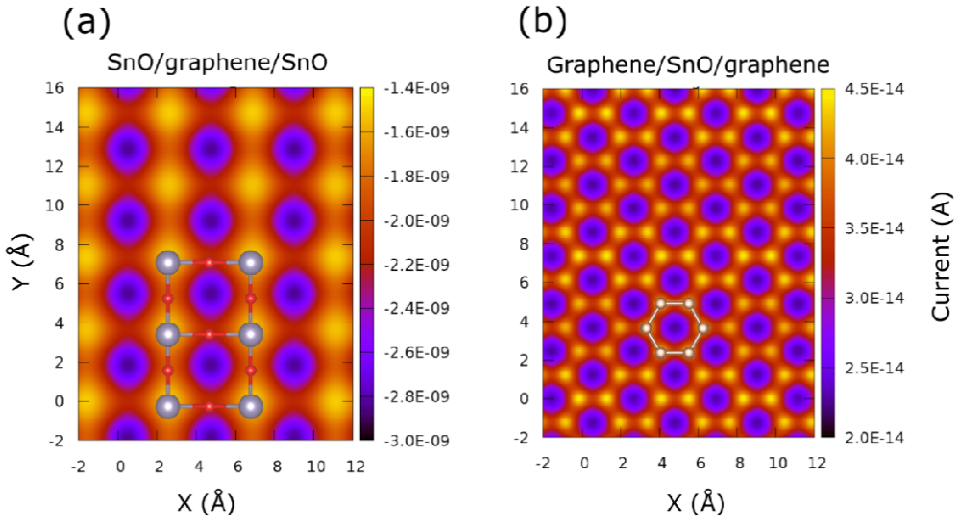

Figure 7. Calculated (constant height) STM images of (a) SnO/graphene/SnO and (b) graphene/SnO/graphene.

4.0 Summary

First principles calculations based on density functional theory were performed on the SnO/graphene heterostructures to investigate the possibility of opening up of graphene's band gap. The results show the presence of a noticeable interaction between the oxide monolayer and graphene opening up a noticeable gap in the SnO/graphene/SnO heterostructure. Moreover, the outer oxide layers appear to shield graphene from the external electric field yielding robustness in graphene's band gap. The diode-like I-V characteristics are predicted for SnO/graphene/SnO, though graphene/SnO/graphene exhibits metallic characteristics. The STM images display characteristics topological images for SnO/graphene heterostructures.

Conflicts of interest

There are no conflicts of interest to declare.

Acknowledgements

Helpful discussion with Kevin Waters, Nabanita Saikia and Max Seel are acknowledged. RAMA and Superior, high performance computing clusters at Michigan Technological University, were used in obtaining results presented in this paper. Helpful support from Dr. S. Gowtham is gratefully acknowledged. This research was partially supported by the Army Research Office through grant number W911NF-14-2-0088.

References:

1. Novoselov, K.S., et al., *Electric field effect in atomically thin carbon films.* science, 2004. **306**(5696): p. 666-669.
2. Ferrari, A.C., et al., *Raman spectrum of graphene and graphene layers.* Physical review letters, 2006. **97**(18): p. 187401.
3. Lee, C., et al., *Measurement of the elastic properties and intrinsic strength of monolayer graphene.* science, 2008. **321**(5887): p. 385-388.
4. Neto, A.C., et al., *The electronic properties of graphene.* Reviews of modern physics, 2009. **81**(1): p. 109.
5. Raccichini, R., et al., *The role of graphene for electrochemical energy storage.* Nature materials, 2014. **14**(3): p. nmat4170.
6. Panchakarla, L.S., et al., *Synthesis, Structure, and Properties of Boron- and Nitrogen-Doped Graphene.* Advanced Materials, 2009: p. NA-NA.
7. Denis, P.A., *Band gap opening of monolayer and bilayer graphene doped with aluminium, silicon, phosphorus, and sulfur.* Chemical Physics Letters, 2010. **492**(4): p. 251-257.
8. Ni, Z.H., et al., *Uniaxial strain on graphene: Raman spectroscopy study and band-gap opening.* ACS Nano, 2008. **2**(11): p. 2301-5.
9. Guinea, F., M.I. Katsnelson, and A.K. Geim, *Energy gaps and a zero-field quantum Hall effect in graphene by strain engineering.* Nature Physics, 2009. **6**(1): p. 30-33.
10. Choi, S.-M., S.-H. Jhi, and Y.-W. Son, *Effects of strain on electronic properties of graphene.* Physical Review B, 2010. **81**(8).
11. Zhou, S.Y., et al., *Substrate-induced bandgap opening in epitaxial graphene.* Nature materials, 2007. **6**(10): p. 770-775.
12. Giovannetti, G., et al., *Substrate-induced band gap in graphene on hexagonal boron nitride:Ab initiodensity functional calculations.* Physical Review B, 2007. **76**(7).
13. Xia, F., et al., *Graphene field-effect transistors with high on/off current ratio and large transport band gap at room temperature.* Nano Lett, 2010. **10**(2): p. 715-8.
14. Zhong, X., et al., *First-principles study of strain-induced modulation of energy gaps of graphene/BN and BN bilayers.* Physical review B, 2011. **83**(19): p. 193403.
15. Li, X., et al., *Graphene/gC 3 N 4 bilayer: considerable band gap opening and effective band structure engineering.* Physical Chemistry Chemical Physics, 2014. **16**(9): p. 4230-4235.
16. Ma, Y., et al., *Graphene adhesion on MoS 2 monolayer: An ab initio study.* Nanoscale, 2011. **3**(9): p. 3883-3887.
17. Padilha, J.E., A. Fazzio, and A.J. da Silva, *Van der Waals heterostructure of phosphorene and graphene: tuning the Schottky barrier and doping by electrostatic gating.* Phys Rev Lett, 2015. **114**(6): p. 066803.
18. Quhe, R., et al., *Tunable and sizable band gap of single-layer graphene sandwiched between hexagonal boron nitride.* NPG Asia Materials, 2012. **4**(2): p. e6.
19. Wang, L., et al., *Negligible environmental sensitivity of graphene in a hexagonal boron nitride/graphene/h-BN sandwich structure.* Acs Nano, 2012. **6**(10): p. 9314-9319.
20. Wang, Z., et al., *Recent Developments in p-Type Oxide Semiconductor Materials and Devices.* Adv Mater, 2016. **28**(20): p. 3831-92.
21. Togo, A., et al., *First-principles calculations of native defects in tin monoxide.* Physical Review

B, 2006. **74**(19): p. 195128.

22. Walsh, A. and G.W. Watson, *Electronic structures of rocksalt, litharge, and herzenbergite SnO by density functional theory.* Physical Review B, 2004. **70**(23): p. 235114.
23. Ogo, Y., et al., *p-channel thin-film transistor using p-type oxide semiconductor, SnO.* Applied Physics Letters, 2008. **93**(3): p. 032113.
24. Saji, K.J., et al., *2D Tin Monoxide-An Unexplored p-Type van der Waals Semiconductor: Material Characteristics and Field Effect Transistors.* Advanced Electronic Materials, 2016. **2**(4): p. 1500453.
25. Daeneke, T., et al., *Wafer-Scale Synthesis of Semiconducting SnO Monolayers from Interfacial Oxide Layers of Metallic Liquid Tin.* ACS Nano, 2017.
26. Du, J., et al., *Electronic characteristics of p-type transparent SnO monolayer with high carrier mobility.* Applied Surface Science, 2017. **401**: p. 114-119.
27. Seixas, L., et al., *Multiferroic Two-Dimensional Materials.* Phys Rev Lett, 2016. **116**(20): p. 206803.
28. Zhang, F., et al., *Two-Dimensional SnO Anodes with a Tunable Number of Atomic Layers for Sodium Ion Batteries.* Nano Lett, 2017. **17**(2): p. 1302-1311.
29. Guo, Q., et al., *Stability and electronic properties of hybrid SnO bilayers: SnO/graphene and SnO/BN.* Nanotechnology, 2017.
30. Zhong, X., et al., *Electronic structure and quantum transport properties of trilayers formed from graphene and boron nitride.* Nanoscale, 2012. **4**(17): p. 5490-8.
31. Perdew, J.P., K. Burke, and M. Ernzerhof, *Generalized Gradient Approximation Made Simple.* Physical Review Letters, 1996. **77**(18): p. 3865-3868.
32. Grimme, S., *Semiempirical GGA-type density functional constructed with a long-range dispersion correction.* J Comput Chem, 2006. **27**(15): p. 1787-99.
33. Kresse, G. and J. Furthmüller, *Efficient iterative schemes for \textit{ab initio} total-energy calculations using a plane-wave basis set.* Physical Review B, 1996. **54**(16): p. 11169-11186.
34. Kresse, G. and J. Furthmüller, *Efficiency of ab-initio total energy calculations for metals and semiconductors using a plane-wave basis set.* Computational Materials Science, 1996. **6**(1): p. 15-50.
35. Moreno, M.S. and R.C. Mercader, *Mössbauer study of SnO lattice dynamics.* Physical Review B, 1994. **50**(14): p. 9875-9881.
36. Meyer, M., et al., *Electronic structure of stannous oxide.* Computational materials science, 1998. **10**(1-4): p. 319-324.
37. Christensen, N., A. Svane, and E.P. y Blancá, *Electronic and structural properties of SnO under pressure.* Physical Review B, 2005. **72**(1): p. 014109.
38. McLeod, J., et al., *Nature of the electronic states involved in the chemical bonding and superconductivity at high pressure in SnO.* JETP letters, 2011. **94**(2): p. 142-146.
39. Govaerts, K., et al., *van der Waals bonding and the quasiparticle band structure of SnO from first principles.* Physical Review B, 2013. **87**(23): p. 235210.
40. Chen, P.-J. and H.-T. Jeng, *Phase diagram of the layered oxide SnO: GW and electron-phonon studies.* 2015. **5**: p. 16359.
41. Yu, Z.G., Y.-W. Zhang, and B.I. Yakobson, *Strain-Robust and Electric Field Tunable Band Alignments in van der Waals WSe2–Graphene Heterojunctions.* The Journal of Physical Chemistry C, 2016. **120**(39): p. 22702-22709.

42. Hod, O., *Interlayer commensurability and superlubricity in rigid layered materials.* Physical Review B, 2012. **86**(7): p. 075444.
43. Malyi, O.I., et al., *Tailoring electronic properties of multilayer phosphorene by siliconization.* Physical Chemistry Chemical Physics, 2018.
44. Klimeš, J., D.R. Bowler, and A. Michaelides, *Chemical accuracy for the van der Waals density functional.* Journal of Physics: Condensed Matter, 2009. **22**(2): p. 022201.
45. Dion, M., et al., *Van der Waals density functional for general geometries.* Physical review letters, 2004. **92**(24): p. 246401.
46. Klimeš, J., D.R. Bowler, and A. Michaelides, *Van der Waals density functionals applied to solids.* Physical Review B, 2011. **83**(19): p. 195131.
47. Kumar, S.B. and J. Guo, *Multilayer graphene under vertical electric field.* Applied Physics Letters, 2011. **98**(22): p. 222101.
48. Wu, B.-R., *Field modulation of the electronic structure of trilayer graphene.* Applied Physics Letters, 2011. **98**(26): p. 263107.
49. Tersoff, J. and D.R. Hamann, *Theory and Application for the Scanning Tunneling Microscope.* Physical Review Letters, 1983. **50**(25): p. 1998-2001.
50. He, H., et al., *Spin-polarized electron transport of a self-assembled organic monolayer on a Ni(111) substrate: An organic spin switch.* Physical Review B, 2006. **73**(19): p. 195311.

Robust band gaps in the graphene/oxide heterostructure– SnO/graphene/SnO

Qing Guo[#], Gaoxue Wang[#], Ravindra Pandey[#] and Shashi P. Karna[##]

[#]Department of Physics, Michigan Technological University, Houghton, Michigan 49931, USA
[##]Weapons and Materials Research Directorate, U.S. Army Research Laboratory, ATTN: RDRL-WM, Aberdeen Proving Ground,
Aberdeen, Maryland 21005-5069, United States

(June 6, 2018)

*Email: pandey@mtu.edu

Abstract

Graphene's applicability in nanoscale devices is somewhat limited because of the absence of a finite band gap. To overcome this limitation of zero band gap, we consider the vertically-stacked heterostructures consisted of graphene and SnO knowing that two-dimensional SnO films were synthesized recently. Calculations based on density functional theory find that the oxide monolayer can induce a noticeable band gap in graphene; the gap is 45 meV in graphene/SnO/graphene and 115 meV in SnO/graphene/SnO heterostructures. Additionally, graphene's band gap can be maintained under a relatively high electric field ($\approx 10^9$ V/m) applied to the heterostructures because of the electrostatic screening effect of the oxide layer. The calculated results suggest relative superiority of the graphene/oxide heterostructures over graphene/BN heterostructures for the nanoscale devices based on graphene.

1.0 Introduction

Graphene has attracted interest due to its remarkable electronic and mechanical properties [1-5], though the absence of a finite band gap has somewhat impeded graphene from practical applications. To overcome this limitation of zero band gap, several approaches including chemical doping [6, 7], mechanical strain [8-10], interlayer interaction with substrate [11, 12], and external electric field [13], have been employed to fabricate graphene-based nanoscale devices. Among these methods, fabrication of a van der Waals (vdW) heterostructure attracts particular attention. For example, opening of a small band gap at K was reported for the graphene/BN bilayer [14]. Other bilayer heterostructures, such as g-C_3N_4/graphene [15], MoS_2/graphene [16], and phosphorene/graphene [17], have also been used to induce the band gap in graphene. Compared to the bilayer heterostructures, the sandwiched trilayer structures have the advantage of not only inducing the band gap, but also providing the environmental stability to the graphene-based heterostructure. For example, a tunable band gap can be opened in the sandwiched BN/graphene/BN structure [18, 19] which could effectively reduce the environmental sensitivity of graphene in the graphene-based devices.

Recently, two-dimensional (2D) tin monoxide (SnO) films with intrinsic p-type semiconducting properties were synthesized [20-22]. A single phase SnO thin film which was fabricated on (001) yttria-stabilized zirconia substrate displayed superior performance in the p-channel thin film transistors [23]. SnO films with thickness of a few atomic layers were also fabricated on sapphire and SiO_2 substrates [24]. Recent experimental efforts include synthesis of the wafer-scale SnO monolayer from the interfacial oxide layers of metallic liquid tin [25]. On the theoretical front, first principles calculations reported the layer-dependence of the electronic properties of SnO films [26]. Calculations also demonstrated that 2D SnO films can be promising candidate for the photocatalytic water splitting [27] and sodium ion battery applications [28]. Our recent theoretical work predicted applicability of the bilayer

configuration composed of the SnO/graphene as field effect transistors (FETs). This is facilitated by a formation of the Schottky contact between the two layers which can tuned from p-type to n-type to Ohmic contact with an external electric field [29].

In this paper, we consider the vertically stacked heterostructures composed of graphene and the oxide monolayer to determine their stability and electronic properties. The considered heterostructures are tri-layers and are expected to be well-suited for device fabrication than the bilayer heterostructure. Our results based on density functional theory show that a band gap as large as 115 meV can be opened in graphene when it is sandwiched between SnO monolayers. Furthermore, we find the finite band gap to be robust under the external electric field up to $\approx 0.3 \times 10^{10}$ V/m. This robustness is found to be due to the electrostatic screening effect of the SnO layers as revealed in the charge density plots. Moreover, the predicted robustness is found to be relatively superior to that predicted for the graphene/BN heterostructure [30] under the applied electric field.

2.0 Computational method

Calculations were performed in the framework of the density functional theory (DFT). The generalized-gradient approximation (GGA) with Perdew-Burk-Ernzerhof (PBE) [31] exchange correlation functional together with Grimme's D2 method [32] representing the van der Waals interaction were employed as implemented in the Vienna ab-initio Simulation Package (VASP) program [33, 34]. We set the energy convergence to 10^{-7} eV and the kinetic energy cut-off to 520 eV. For the structural optimization, we use a grid of (5×3×1) k-points for sampling in reciprocal space. The criterion for force convergence was set to less than 0.01 eV/Å on each atom. For electronic properties calculations including total energy and density of states (DOS), we used a much denser k-points grid of (33×17×1). To eliminate the interaction between replicas due to periodic boundary conditions, a large vacuum layer more than 15 Å is built in the out-plane direction.

Calculations of the oxide/graphene heterostructures were performed in the context of the commensurate lattice approximation using graphene as a reference lattice. The periodic supercell was consisted of (1×3) cell for graphene and (1×2) cell for the SnO monolayer. The lattice mismatch between the oxide monolayer and graphene induced elongation (shortening) along x-(y-) direction in the oxide monolayer. A comparison of the results obtained using the (7×3) graphene/(8×2) SnO supercell and (1×3) graphene/(1×2) SnO supercell found the smaller supercell to reproduce very well structure and electronic properties of the bilayer heterostructure [29]. Note that the position of the Dirac point depends on how we choose the shape or size of the supercell for calculations. In our work, we have used rectangular 12-atom unit cell, and that there exists zero band gap for the freestanding graphene in this rectangular cell, thus confirming that the k-points grid is large enough to ensure the accuracy of calculations (Fig S2, Supplementary Information).

The calculated structural and electronic properties of the pristine SnO bulk [29] agree well with the previously reported experimental [24, 35] and theoretical results [22, 36-40] affirming the accuracy and reliability of the modeling elements employed in this study. It is to be noted that the heterostructures with a noticeable lattice mismatch have been predicted to have novel properties such as phosphorene/graphene [17] and WSe_2/graphene [41].

3.0 Results and discussions

3.1 Structural properties:

The geometrical configurations of the vertically-stacked heterostructures, namely SnO/graphene/SnO and graphene/SnO/graphene are shown in Fig. 1. Following the stacking nomenclature of graphite, the ABA-stacked configuration is composed of the AB-stacked bilayers displaying mirror symmetry relative to the central layer. The AAA-stacked configuration is composed of the AA-stacked bilayers on both side of the central layer. And the ABC-stacked configuration is composed of the AB-stacked bilayer on one side and the AA-stacked bilayer on the other side of the central layer. Initially, the registry index RI method [42] was employed to search the lowest energy

configurations for SnO/graphene bilayer as discussed in our previous work [29]. The results of the bilayer structures were then used to construct the trilayer configurations as shown in Figure 1. The total energy of the trilayer configuration was calculated with respect to displacement of the graphene layer. The ABA-stacked trilayer is found to be the energetically preferred configuration as displayed in Figure S2 (Supplementary Information).

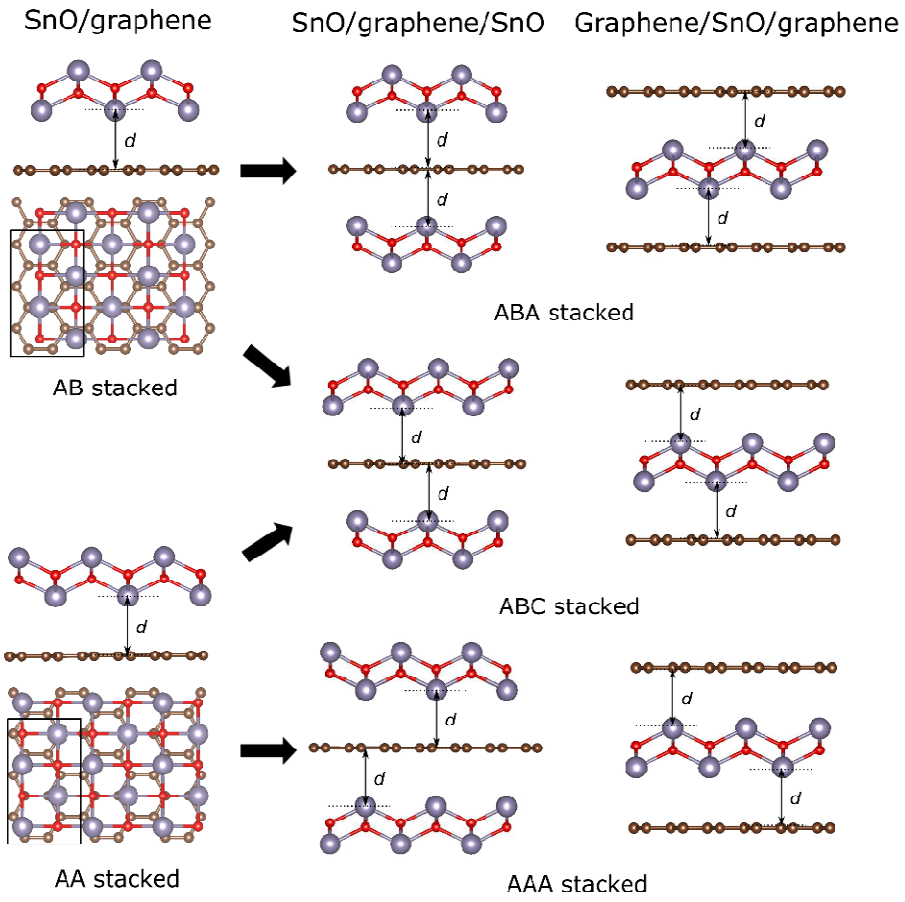

Figure 1. The stacking configurations of SnO/graphene heterostructures considered. Color code: C: small brown sphere, Sn: large grey sphere and O: small red sphere.

Table 1 lists the calculated structural properties and the band gap of SnO/graphene heterostructures. Not surprisingly, the ABA-stacked configuration is more energetically stable for the SnO/graphene/SnO and graphene/SnO/graphene heterostructures. In the ABA-stacked configuration with the mirror symmetry, the

interlayer distances are very similar: ≈3.46 Å for SnO/graphene/SnO and ≈3.42 Å for graphene/SnO/graphene. In the AAA-stacked configuration, the interlayer distance is ≈3.48 Å, very close to the interlayer distance of 3.47 Å calculated for the AA-stacked bilayer [23]. While in the ABC stacked mode, the interlayer space is 3.42 Å on the 'AB-stacked' side and 3.45 Å on the 'BC-stacked' side. This is similar to what has been calculated for the constituent bilayers: 3.42 Å for AB-stacked and 3.47 Å for the AA-stacked bilayers. The intralayer bond distances, R_{Sn-O} and $R_{C-C,}$ are calculated to be 2.35 (2.24) Å and 1.42 (1.41) Å in x- (y-) direction, respectively. Note that bulk SnO has a tetragonal PbO layered structure with the interlayer distance of 2.48 Å [23].

The DFT results show that the heterostructures follow the trend in stability as predicted for the bilayers [23] with ABA-stacked heterostructure being energetically preferred. Additionally, the binding energy of a heterostructure is slightly higher than the sum of binding energies of the constituent bilayers suggesting that the stable oxide/graphene heterostructures can be fabricated. A comparison of SnO/graphene/SnO and graphene/SnO/graphene heterostructures within the same stacking mode finds the latter heterostructure to have a smaller binding energy. This is due to the fact that the SnO monolayer owns a certain thickness which enlarges the distance between two graphene layers thus reducing contributions from the interlayer interactions. For example, the calculated distance between two graphene layers in ABA-stacked graphene/SnO/graphene is 9.1 Å while distance between the oxide layers in ABA-stacked SnO/graphene/SnO is 6.9 Å.

Table 1. Calculated binding energy ($E_{binding}$), interlayer spacing ($d_{interlayer}$) and band gap (E_{gap}) of SnO/graphene heterostructures.

Heterostructure	Stacking configuration	$E_{binding}$ / unit cell (eV)	$d_{interlayer}$ (Å)	E_{gap} (meV)
SnO/graphene	AB	0.484	3.42	8
SnO/graphene	AA	0.460	3.47	-
SnO/graphene/SnO	ABA	0.993	3.46, 3.45	115
SnO/graphene/SnO	ABC	0.987	3.42, 3.45	34
SnO/graphene/SnO	AAA	0.955	3.48, 3.47	58
graphene/SnO/graphene	ABA	0.969	3.42, 3.43	45
graphene/SnO/graphene	ABC	0.983	3.42, 3.45	7
graphene/SnO/graphene	AAA	0.925	3.48, 3.47	68

3.2 Electronic properties

To simulate SnO/graphene/SnO trilayer, we have employed rectangular unit cell containing 12 carbon atoms for which the high-symmetric points are indicated by X, Y and S points in the first Brillouin zone (BZ) (Fig S2, Supplementary Information). In this k-point setup, the band structure of free-standing graphene (Fig. 2(a)) is displayed showing that the Dirac point of free-standing graphene is located at the Γ for the rectangular 12-atom unit cell. Figs. 2(b), 2(c) and 2(d) displays the band structures of the energetically preferred configurations of the SnO/graphene/SnO and graphene/SnO/. The high symmetry points in the first BZ of the rectangular supercell are shown in the inset of Fig 2(a).

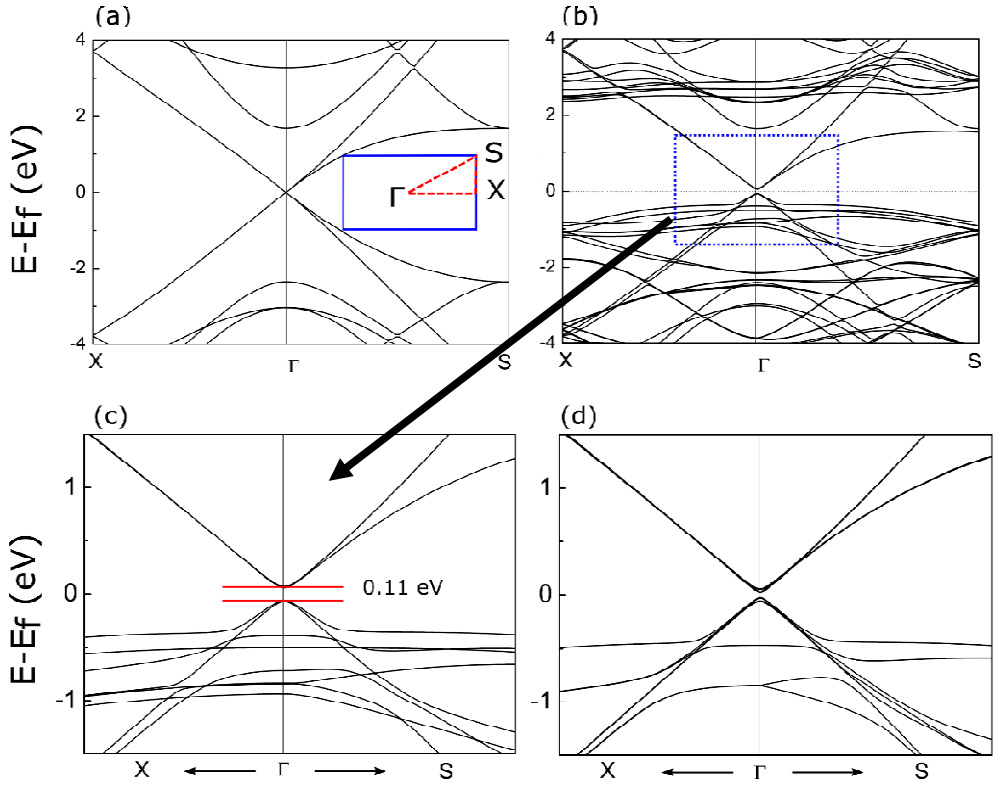

Figure 2. Calculated band structures of (a) free-standing graphene and (b) ABA stacking SnO/graphene/SnO heterostructure (c) zoom-in band structures around Γ indicated by the blue dash line box in 2 (b), and (d) graphene/SnO/graphene heterostructure.

In the ABA-stacked SnO/graphene/SnO heterostructure, a noticeable finite band gap of 115 meV is opened up in graphene which is about two times of that predicted for the ABA-stacked BN/graphene/BN heterostructure [30]. Note that calculations using the hybrid functional HSE06 yieldthe band gap to be 240 meV. Such a large gap opening is mainly due to interaction between the oxide layers and graphene which breaks the equivalence in carbon sublattice of graphene. This unequal interaction is clearly illustrated by the partial charge density plots displayed in Fig. 3 (a).

In Fig. 3 (a), the partial charge density is plotted in the energy range from -1 eV to 0 eV (i.e. Fermi energy) and the isosurface in the 3D plot is 0.02 e/Å ^{3}. Slice 1, 2, 3 are the 2D views sliced at the positions of different carbon atoms indicated in the 3D partial charge density plot. From 2D view of the slices, we can clearly see that C

atoms which are beneath Sn atoms (slice 1) interact more strongly than the other C atoms (slice 2, 3), and the interaction is enhanced by the presence of the mirror-symmetric oxide layer. Likewise, the charge density difference plots shown in Fig. S3 (Supplementary Information) confirm the presence of interaction between graphene and the oxide monolayer.

In contrast, a loss of mirror-symmetric layer for the ABC-stacked heterostructure leads to a smaller degree of interaction yielding the gap opening of ≈34 meV. This is also the case with the graphene/SnO/graphene heterostructure for which absence of a mirror-symmetric layer in the ABC-stacked configuration leads to a smaller degree of C-Sn atomic interaction yielding a negligible gap opening of ≈7 meV (Table 1).

The extent of the interlayer interaction in the heterostructures can also be seen in the electron localization function (ELF) plots given in Fig. 3 (b). For the ABA-stacked SnO/graphene/SnO heterostructure, deformation of the Sn atom's lone pair sphere facing C atom is mainly due to a higher degree of the interlayer interaction in the heterostructure. Note that the ELF sphere is associated with the lone pair formed by Sn ($5p_z$) and Sn (5s)-O($2p_z$) orbitals at the oxide monolayer surface [22].

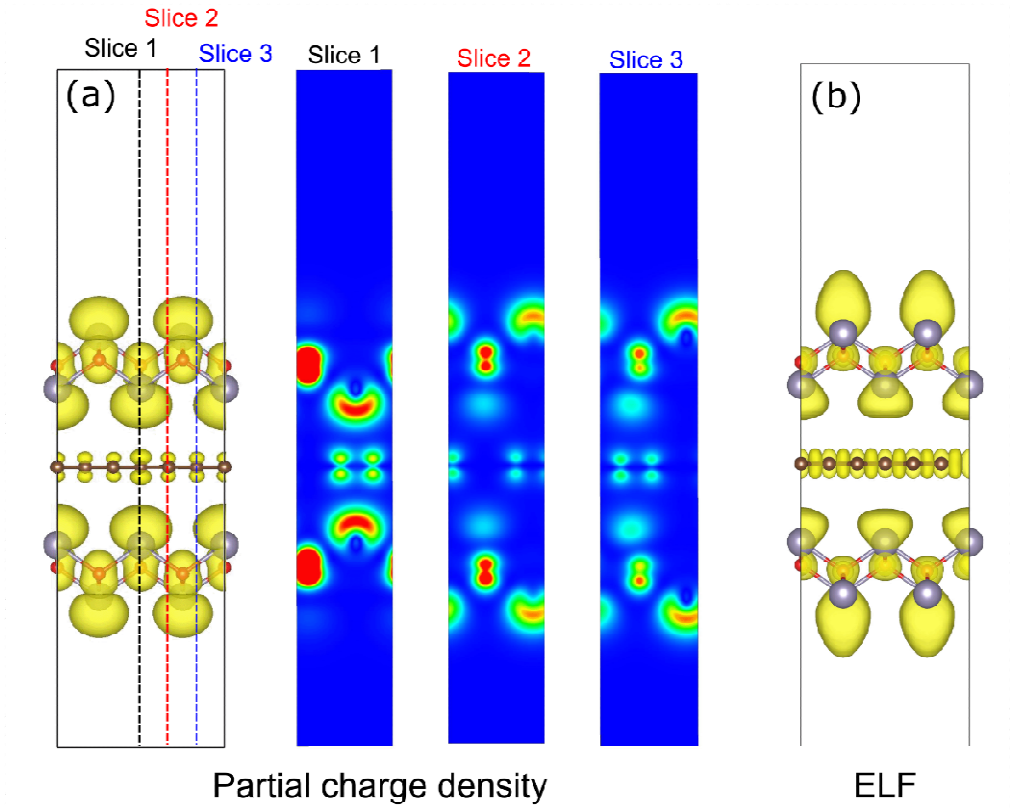

Figure 3. ABA-stacked SnO/graphene/SnO heterostructure: (a) the partial charge density plots in the energy range from -1 eV to 0 (i.e. Fermi energy) with the iso-surface of 0.02 e/Å ^{3}. 2D slices indicated by the black, red and blue lines are also plotted. (b) ELF with the isosurface value of 0.8.

To determine the sensitivity of our results on the functional forms describing vdW interactions, we perform a limited set of calculations using optB88-vdW functional form [43-46]. The results show that stability and opening of the band gap do not sensitively depend on the way we describe vdW interactions in these trilayer configurations (Tables. S1 and S2, Supplementary Information).

3.3 Effect of the tensile/compressive strain applied to heterostructures.

To affirm the fact that the interaction between the oxide monolayer and graphene in the heterostructure is the cause of opening of the graphene's band gap, additional calculations were performed on the heterostructures applying the perpendicular strain ranging from -10% to +10%. The results are shown in Fig. 4 (a). Interestingly, the

graphene's band gap increases to 140 meV for the compressive strain of 8% (i.e. $d_{interlayer}$=3.16 Å). On the other hand, application of the perpendicular tensile strain of about 9% (i.e. $d_{interlayer}$=3.78 Å) yields the band gap of 74 meV suggesting the reduced degree of interaction between the oxide monolayer and graphene.

The orbital projected band structures shown in Fig. 4 (b)~(d) for the case of the perpendicular compressive strain of 8% find lifting of degeneracy in the conduction levels of graphene. The lone pair at the SnO monolayer surface formed by Sn ($5p_z$) and Sn (5s)-O($2p_z$) orbitals [22] overlaps with C ($2p_z$) orbitals and induces a strong interaction between the two layers in the heterostructure.

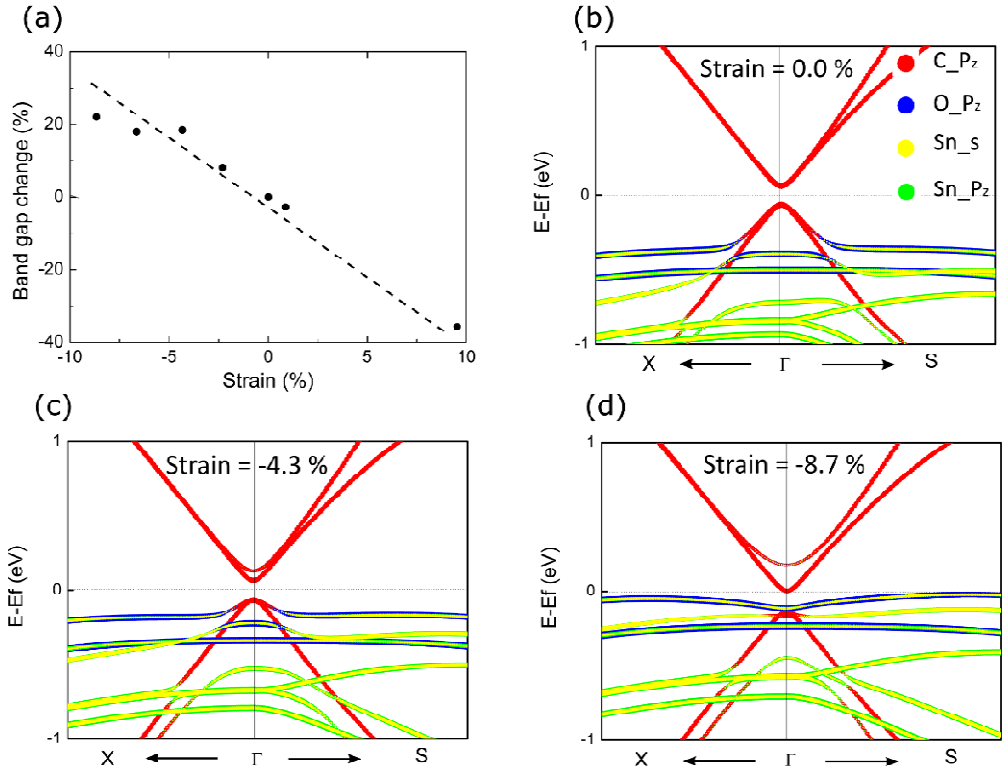

Figure 4. ABA-stacked SnO/graphene/SnO heterostructure: (a) calculated band gap of graphene as a function of strain applied perpendicular to the heterostructure. (b), (c) and (d) the projected band structures around Γ associated with the perpendicular strain of 0%, -4.3% and -8.7%. In (b), (c) and (d), the red, blue, yellow and green lines show the orbital projected C_p_z, O_p_z, Sn_s and Sn_p_z bands, respectively

3.3 Effect of the external electric field on the heterostructures

The electric field is applied vertically along the stacked direction of the

heterostructure. Fig. 5 (a) displays variation in the band gap with the applied electric field for the ABA-stacked heterostructures. Remarkably, the band gap is found to be independent of the electric field up to 3×10^9 V/m for SnO/graphene/SnO heterostructure. It should be pointed out that the electric field at the order of ~10^9 V/m is within the range of the fabricated devices. In contrast, although a band gap is induced in graphene trilayer by applying electric field, it is not stable; the band gap opens up to its maxima at the electric field of 0.5×10^9 V/m and then begins to close with the increase in the electric field [47, 48]. A similar results has also been seen for the graphene/BN/graphene heterostructure where opening of the band gap of graphene is only 57 meV for the electric field of 1×10^9 V/m [30].

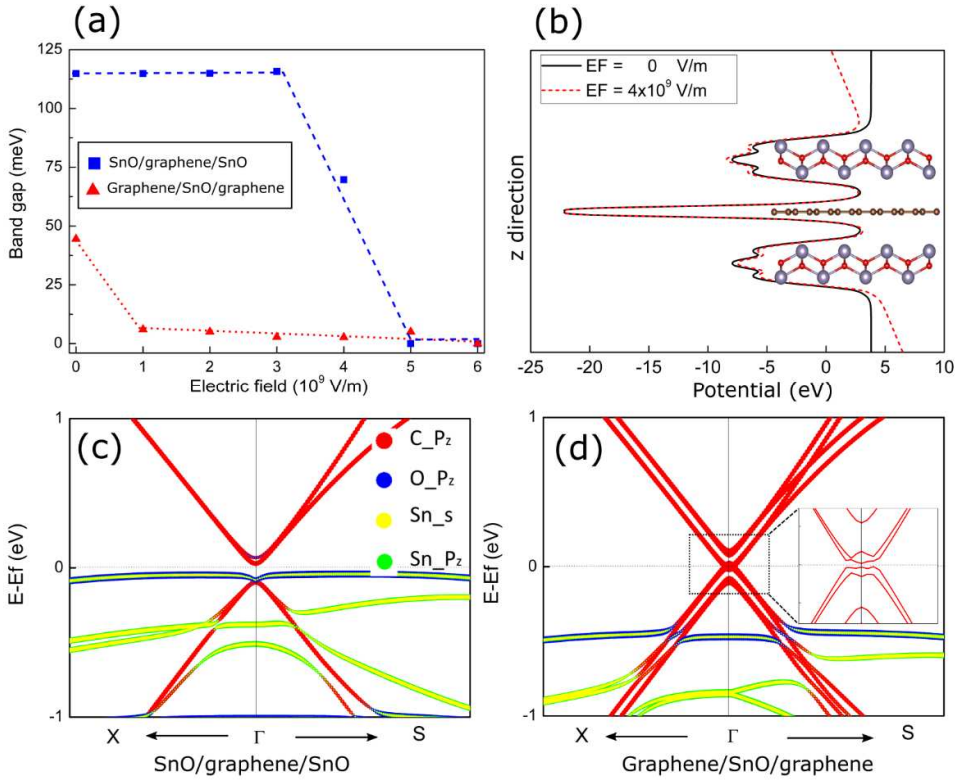

Figure 5: ABA-stacked SnO/graphene heterostructures: (a) calculated band gap as a function of the applied electric field. (b) Planar average electrostatic potential along the z-direction. Color code: Black line, E_F=0 and red dot line. $E_F=4 \times 10^9$ V/m. (c) Projected band structure around Γ at $E_F=4 \times 10^9$ V/m for SnO/graphene/SnO. (d) Projected band structure around Γ at $E_F= 1 \times 10^9$ V/m for graphene/SnO/graphene. In (c) and (d), the red, blue, yellow and green lines stand for the orbital projected C_p_z, O_p_z, Sn_s and Sn_p_z bands, respectively

Our calculations find that application of an external electric field from bottom to top leads to upward shift of VBM of top SnO layer, while lowering that of the bottom SnO layer in SnO/graphene/SnO. The middle graphene layer appears to be relatively unaffected. However, when the electric field becomes larger than 3×10^9 V/m, VBM of top SnO layer is higher than that of graphene's, yielding the gap to be between VBM of top SnO layer and CBM of graphene layer (Fig. 5 (c)). A further increase of the electric field then induces decrease in the heterostructure's band gap due to the stark effect till the band gap closes for the electric field of $\sim5\times10^9$ V/m (Fig. 5(a)).

To further understand this robustness of the band gap under such a high electric field, the planar average electrostatic potential is plotted in Fig. 5 (b). We find that a wide barrier of the outer oxide layers is essentially shield graphene. This is not the case with the graphene/SnO/graphene heterostructure for which the outer graphene layers are directly exposed to the external electric field thereby closing the gap. The Dirac point of graphene on the higher potential side goes below Fermi level while the Dirac point of the other graphene layer goes above Fermi level as shown in Fig. 5 (d) and overlap of Dirac cones yields nearly zero band gap under the external electric field.

Additional calculations have been carried out to illustrate the influence of SnO substrate's thickness on the electronic properties of the heterostructure. For the ABAA-stacked structure consisted of SnO monolayer/ graphene/SnO bilayer and ABAAA- stacked structure consisted of SnO monolayer/ graphene/ SnO trilayer, the results show that top of the valence band associated with SnO layers have risen to the Fermi level with the increase in the substrate thickness. Consequently, the band gap is closed in graphene/oxide heterostructures with a thicker SnO substrate which will result in an Ohmic conductivity of the device (Fig S4, Supplementary Information)

3.4 Electronic transport properties

Next, we calculate the I-V characteristics of the SnO/graphene heterostructure using the scanning tunneling microscope (STM) setup [29]. The tunneling current from the sample to the tip is obtained using the Tersoff and Hamann approximation

[49] taking account of the effect of thermally excited electrons as proposed by He *et al*. [50]. We define the bias to be positive when the sample is connected to a positive potential and electrons tunnel from the tip to the sample. The tip is considered to be separated from the sample by a vacuum barrier width of 5 Å, mimicking a non-bonded tip configuration for the STM measurements. It is to be noted that the tunneling current depends exponentially on the separation of the tip to sample. Therefore, the choice of tip-sample separation will determine the magnitude of the tunneling current, but should not affect the predicted trend for the assembled monolayers considered. In calculations, a finite Au_{13} cluster with the icosahedral shape was used to simulate the tip, and the tunneling current is essentially an integration of the convolution of density of states (DOS) of the tip and sample, and will depend on the valence and conduction states near the Fermi level of a given heterostructure.

Fig. 6 (a) displays a comparison of the I-V characteristics of the SnO/graphene heterostructures. The inset is the zoomed figure in the red rectangular box showing that the graphene/SnO/graphene heterostructure behaves like a good conductor. This is caused by the nearly zero band gap of graphene, thus the electron tunneling between the tip and the top graphene layer occurs at a very small bias field. While for the other two heterostructures (i.e. SnO/graphene and SnO/graphene/SnO), since the electron tunnels between the tip and the top SnO layer, the I-V characteristics show diode-like characteristics due to the band gap of the SnO monolayer. We also notice that the breakdown voltage of SnO/graphene/SnO is lower than that of the SnO/graphene bilayer. This is due to fact that the Schottky barrier of the trilayer is about 0.1 eV lower relative to that in the bilayer.

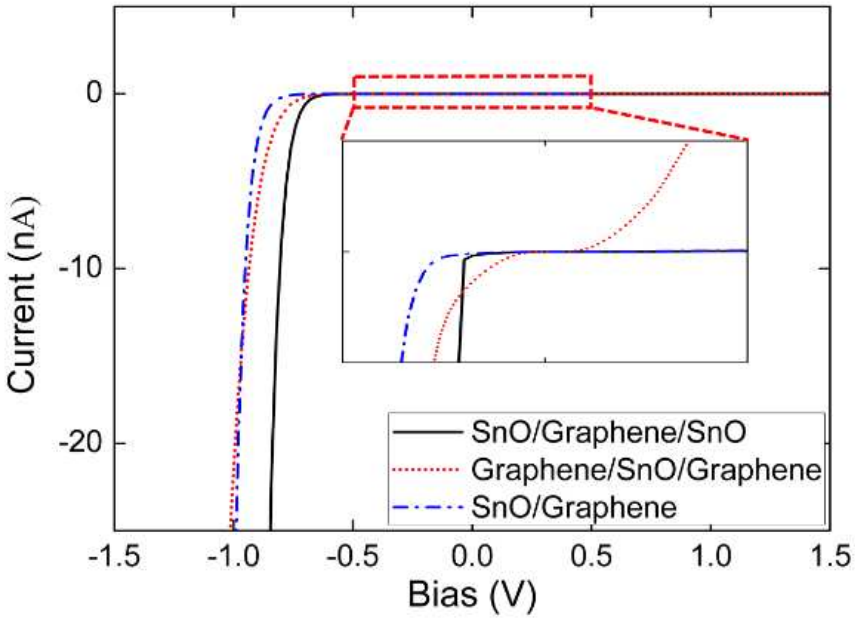

Figure 6: Calculated I-V characteristics of SnO/graphene heterostructures.

The topology of the heterostructures can be characterized by the simulated STM images and (14×18) $Å^2$ images of SnO/graphene heterostructures are displayed in Fig. 7 obtained in the constant height mode with the tip distance of 3 Å. For SnO/graphene/SnO, the top Sn atoms are associated with the bright regions whereas the top carbon rings in graphene/SnO/graphene are clearly seen.

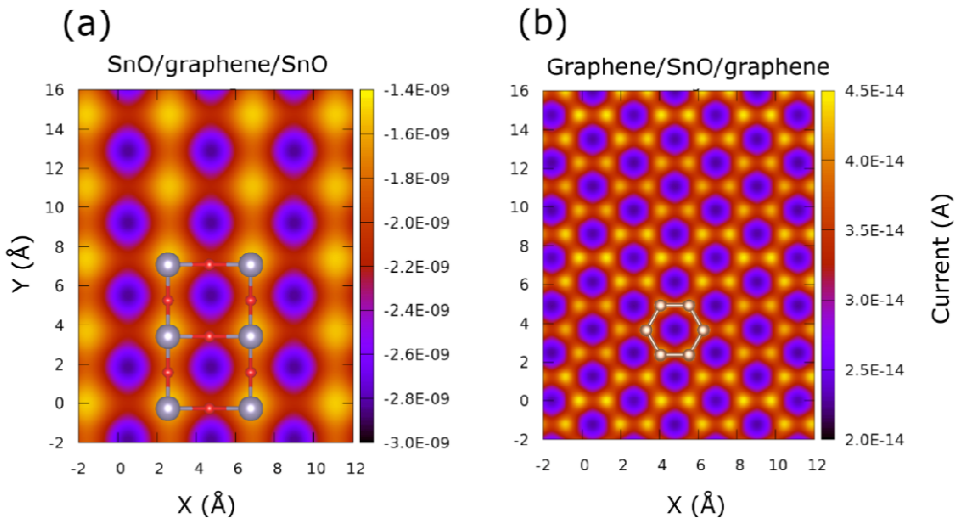

Figure 7. Calculated (constant height) STM images of (a) SnO/graphene/SnO and (b) graphene/SnO/graphene.

4.0 Summary

First principles calculations based on density functional theory were performed on the SnO/graphene heterostructures to investigate the possibility of opening up of graphene's band gap. The results show the presence of a noticeable interaction between the oxide monolayer and graphene opening up a noticeable gap in the SnO/graphene/SnO heterostructure. Moreover, the outer oxide layers appear to shield graphene from the external electric field yielding robustness in graphene's band gap. The diode-like I-V characteristics are predicted for SnO/graphene/SnO, though graphene/SnO/graphene exhibits metallic characteristics. The STM images display characteristics topological images for SnO/graphene heterostructures.

Conflicts of interest

There are no conflicts of interest to declare.

Acknowledgements

Helpful discussion with Kevin Waters, Nabanita Saikia and Max Seel are acknowledged. RAMA and Superior, high performance computing clusters at Michigan Technological University, were used in obtaining results presented in this paper. Helpful support from Dr. S. Gowtham is gratefully acknowledged. This research was partially supported by the Army Research Office through grant number W911NF-14-2-0088.

References:

1. Novoselov, K.S., et al., *Electric field effect in atomically thin carbon films.* science, 2004. **306**(5696): p. 666-669.
2. Ferrari, A.C., et al., *Raman spectrum of graphene and graphene layers.* Physical review letters, 2006. **97**(18): p. 187401.
3. Lee, C., et al., *Measurement of the elastic properties and intrinsic strength of monolayer graphene.* science, 2008. **321**(5887): p. 385-388.
4. Neto, A.C., et al., *The electronic properties of graphene.* Reviews of modern physics, 2009. **81**(1): p. 109.
5. Raccichini, R., et al., *The role of graphene for electrochemical energy storage.* Nature materials, 2014. **14**(3): p. nmat4170.
6. Panchakarla, L.S., et al., *Synthesis, Structure, and Properties of Boron- and Nitrogen-Doped Graphene.* Advanced Materials, 2009: p. NA-NA.
7. Denis, P.A., *Band gap opening of monolayer and bilayer graphene doped with aluminium, silicon, phosphorus, and sulfur.* Chemical Physics Letters, 2010. **492**(4): p. 251-257.
8. Ni, Z.H., et al., *Uniaxial strain on graphene: Raman spectroscopy study and band-gap opening.* ACS Nano, 2008. **2**(11): p. 2301-5.
9. Guinea, F., M.I. Katsnelson, and A.K. Geim, *Energy gaps and a zero-field quantum Hall effect in graphene by strain engineering.* Nature Physics, 2009. **6**(1): p. 30-33.
10. Choi, S.-M., S.-H. Jhi, and Y.-W. Son, *Effects of strain on electronic properties of graphene.* Physical Review B, 2010. **81**(8).
11. Zhou, S.Y., et al., *Substrate-induced bandgap opening in epitaxial graphene.* Nature materials, 2007. **6**(10): p. 770-775.
12. Giovannetti, G., et al., *Substrate-induced band gap in graphene on hexagonal boron nitride:Ab initiodensity functional calculations.* Physical Review B, 2007. **76**(7).
13. Xia, F., et al., *Graphene field-effect transistors with high on/off current ratio and large transport band gap at room temperature.* Nano Lett, 2010. **10**(2): p. 715-8.
14. Zhong, X., et al., *First-principles study of strain-induced modulation of energy gaps of graphene/BN and BN bilayers.* Physical review B, 2011. **83**(19): p. 193403.
15. Li, X., et al., *Graphene/gC 3 N 4 bilayer: considerable band gap opening and effective band structure engineering.* Physical Chemistry Chemical Physics, 2014. **16**(9): p. 4230-4235.
16. Ma, Y., et al., *Graphene adhesion on MoS 2 monolayer: An ab initio study.* Nanoscale, 2011. **3**(9): p. 3883-3887.
17. Padilha, J.E., A. Fazzio, and A.J. da Silva, *Van der Waals heterostructure of phosphorene and graphene: tuning the Schottky barrier and doping by electrostatic gating.* Phys Rev Lett, 2015. **114**(6): p. 066803.
18. Quhe, R., et al., *Tunable and sizable band gap of single-layer graphene sandwiched between hexagonal boron nitride.* NPG Asia Materials, 2012. **4**(2): p. e6.
19. Wang, L., et al., *Negligible environmental sensitivity of graphene in a hexagonal boron nitride/graphene/h-BN sandwich structure.* Acs Nano, 2012. **6**(10): p. 9314-9319.
20. Wang, Z., et al., *Recent Developments in p-Type Oxide Semiconductor Materials and Devices.* Adv Mater, 2016. **28**(20): p. 3831-92.
21. Togo, A., et al., *First-principles calculations of native defects in tin monoxide.* Physical Review

B, 2006. **74**(19): p. 195128.

22. Walsh, A. and G.W. Watson, *Electronic structures of rocksalt, litharge, and herzenbergite SnO by density functional theory.* Physical Review B, 2004. **70**(23): p. 235114.
23. Ogo, Y., et al., *p-channel thin-film transistor using p-type oxide semiconductor, SnO.* Applied Physics Letters, 2008. **93**(3): p. 032113.
24. Saji, K.J., et al., *2D Tin Monoxide-An Unexplored p-Type van der Waals Semiconductor: Material Characteristics and Field Effect Transistors.* Advanced Electronic Materials, 2016. **2**(4): p. 1500453.
25. Daeneke, T., et al., *Wafer-Scale Synthesis of Semiconducting SnO Monolayers from Interfacial Oxide Layers of Metallic Liquid Tin.* ACS Nano, 2017.
26. Du, J., et al., *Electronic characteristics of p-type transparent SnO monolayer with high carrier mobility.* Applied Surface Science, 2017. **401**: p. 114-119.
27. Seixas, L., et al., *Multiferroic Two-Dimensional Materials.* Phys Rev Lett, 2016. **116**(20): p. 206803.
28. Zhang, F., et al., *Two-Dimensional SnO Anodes with a Tunable Number of Atomic Layers for Sodium Ion Batteries.* Nano Lett, 2017. **17**(2): p. 1302-1311.
29. Guo, Q., et al., *Stability and electronic properties of hybrid SnO bilayers: SnO/graphene and SnO/BN.* Nanotechnology, 2017.
30. Zhong, X., et al., *Electronic structure and quantum transport properties of trilayers formed from graphene and boron nitride.* Nanoscale, 2012. **4**(17): p. 5490-8.
31. Perdew, J.P., K. Burke, and M. Ernzerhof, *Generalized Gradient Approximation Made Simple.* Physical Review Letters, 1996. **77**(18): p. 3865-3868.
32. Grimme, S., *Semiempirical GGA-type density functional constructed with a long-range dispersion correction.* J Comput Chem, 2006. **27**(15): p. 1787-99.
33. Kresse, G. and J. Furthmüller, *Efficient iterative schemes for \textit{ab initio} total-energy calculations using a plane-wave basis set.* Physical Review B, 1996. **54**(16): p. 11169-11186.
34. Kresse, G. and J. Furthmüller, *Efficiency of ab-initio total energy calculations for metals and semiconductors using a plane-wave basis set.* Computational Materials Science, 1996. **6**(1): p. 15-50.
35. Moreno, M.S. and R.C. Mercader, *Mössbauer study of SnO lattice dynamics.* Physical Review B, 1994. **50**(14): p. 9875-9881.
36. Meyer, M., et al., *Electronic structure of stannous oxide.* Computational materials science, 1998. **10**(1-4): p. 319-324.
37. Christensen, N., A. Svane, and E.P. y Blancá, *Electronic and structural properties of SnO under pressure.* Physical Review B, 2005. **72**(1): p. 014109.
38. McLeod, J., et al., *Nature of the electronic states involved in the chemical bonding and superconductivity at high pressure in SnO.* JETP letters, 2011. **94**(2): p. 142-146.
39. Govaerts, K., et al., *van der Waals bonding and the quasiparticle band structure of SnO from first principles.* Physical Review B, 2013. **87**(23): p. 235210.
40. Chen, P.-J. and H.-T. Jeng, *Phase diagram of the layered oxide SnO: GW and electron-phonon studies.* 2015. **5**: p. 16359.
41. Yu, Z.G., Y.-W. Zhang, and B.I. Yakobson, *Strain-Robust and Electric Field Tunable Band Alignments in van der Waals WSe2–Graphene Heterojunctions.* The Journal of Physical Chemistry C, 2016. **120**(39): p. 22702-22709.

42. Hod, O., *Interlayer commensurability and superlubricity in rigid layered materials.* Physical Review B, 2012. **86**(7): p. 075444.
43. Malyi, O.I., et al., *Tailoring electronic properties of multilayer phosphorene by siliconization.* Physical Chemistry Chemical Physics, 2018.
44. Klimeš, J., D.R. Bowler, and A. Michaelides, *Chemical accuracy for the van der Waals density functional.* Journal of Physics: Condensed Matter, 2009. **22**(2): p. 022201.
45. Dion, M., et al., *Van der Waals density functional for general geometries.* Physical review letters, 2004. **92**(24): p. 246401.
46. Klimeš, J., D.R. Bowler, and A. Michaelides, *Van der Waals density functionals applied to solids.* Physical Review B, 2011. **83**(19): p. 195131.
47. Kumar, S.B. and J. Guo, *Multilayer graphene under vertical electric field.* Applied Physics Letters, 2011. **98**(22): p. 222101.
48. Wu, B.-R., *Field modulation of the electronic structure of trilayer graphene.* Applied Physics Letters, 2011. **98**(26): p. 263107.
49. Tersoff, J. and D.R. Hamann, *Theory and Application for the Scanning Tunneling Microscope.* Physical Review Letters, 1983. **50**(25): p. 1998-2001.
50. He, H., et al., *Spin-polarized electron transport of a self-assembled organic monolayer on a Ni(111) substrate: An organic spin switch.* Physical Review B, 2006. **73**(19): p. 195311.

Supplementary Information for
Robust band gaps in the graphene/oxide heterostructure– SnO/graphene/SnO

Qing Guo[#], Gaoxue Wang[#], Ravindra Pandey[#] and Shashi P. Karna[##]

[#]Department of Physics, Michigan Technological University, Houghton, Michigan 49931, USA
[##]Weapons and Materials Research Directorate, U.S. Army Research Laboratory, ATTN: RDRL-WM, Aberdeen Proving Ground,
Aberdeen, Maryland 21005-5069, United States

(June 6, 2018)

*Email: pandey@mtu.edu

S1: Brillouin zone of rectangular 12-atom unit cell

The position of the Dirac point depends on how we choose the shape or size of the supercell for calculations. In our work, we have used rectangular 12-atom unit cell for the SnO/graphene/SnO trilayer.

Figure S1 displays graphene's first Brillouin zone of the Wigner-Seitz 2-atom unit cell (shaded area), rectangular 4-atom unit cell (large black) and rectangular 12-atom unit cell (small red). As discussed in Suzuki's paper (2017, J of Modern Physics, 8, 607-621), the K and K' points of the Wigner-Seitz 2-atom unit cell are folded to Q and P points for the rectangular 4-atom unit cell. In our calculation, we used a unit cell 3 times of the 4-atom unit cell in Y direction (Figure S2(a)) which will reduce the b_2 vector to 1/3 in the reciprocal space while keeping b_1 vector the same (show in Figure S1(b), red rectangular). The P and Q-points of the rectangular 4-atom unit cell are now folded to Γ point, while the Y' point is folded to Y point, the W point is folded to S point and the X point remains the same.

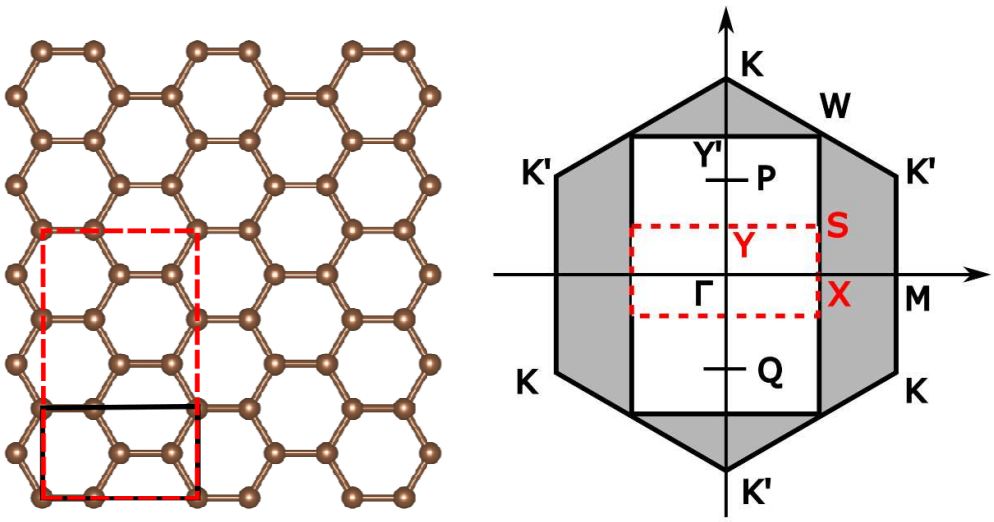

Figure S1 (a) The unit cell of graphene consisted of rectangular 4-atom unit cell (black line) and rectangular 12-atom unit cell (red dash line, this work) (b) The first Brillouin zone of the Wigner-Seitz 2-atom unit cell (shaded area), rectangular 4-atom unit cell (large black) [1]and rectangular 12-atom unit cell (small red). The high-symmetric points within the rectangular unit cell are indicated by, X, Y, W and S within the reciprocal lattice plane.

S2: Potential energy surface of the SnO/graphene/SnO

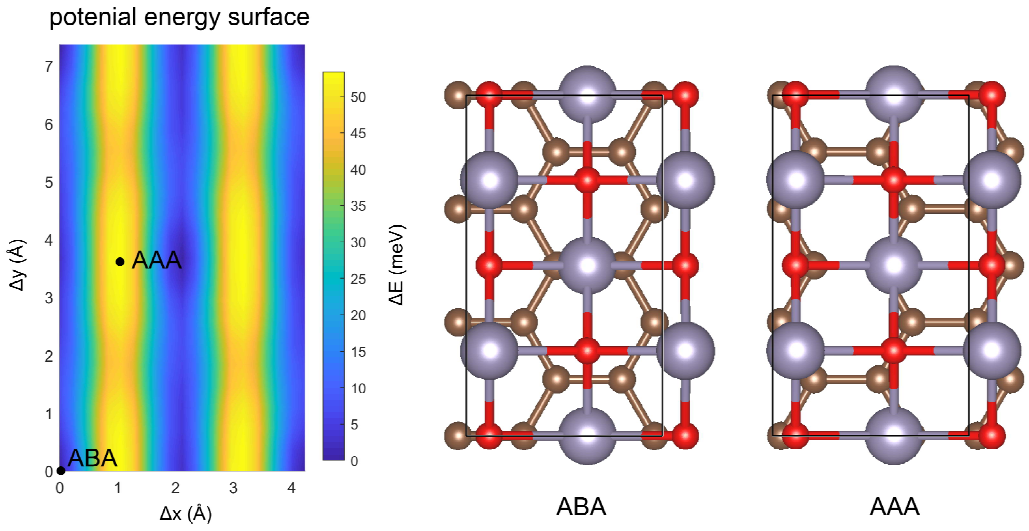

Figure S2. Calculated energy surface of shifting the graphene layer in the SnO/graphene/SnO trilayer configurations. Δx, Δy represent the displacement with respect to the ABA-stacked configuration.

S3. Charge density difference of ABA -stacked SnO/graphene/SnO tri-layer

The charge density difference is derived using the following formula:

ΔCHG = CHG_total – (CHG_topSnO + CHG_graphene + CHG_bottom_SnO).

Here, "total" is the tri-layer structure, "top_SnO" is the top SnO monolayer, "graphene" is the middle layer and "bottom_SnO" indicates the bottom SnO monolayer.

The charge density difference is mainly due to the shape deformation of electron clouds which belong to different layers at the interface. Note that the contact in the trilayer configuration is a semiconductor-graphene contact. So, unlike the metal-graphene contact in the reference [2], there exists no extra unoccupied orbitals below the Fermi level of the heterostructure leading to absence of the p-doping at the interface.

Fig. S3 (b) shows the planar average charge density difference along the z-direction indicating occurrence of the charge space distribution variation compare

with the original SnO layers and graphene. A side- view of charge density difference plot in Fig. S3 (c) depicts this charge density difference in a more intuitive way: the blue regions around C atoms indicate reduction of electrons to the adjacent Sn atoms which are surrounded by the yellow regions. Asymmetry in the charge transfer is shown in the top view of charge density difference in Fig. S3 (c): a higher degree of the charge reduction around carbon atoms which are adjacent to Sn atoms with respect to carbon atoms which are far away from Sn atoms. This asymmetric charge distribution variation in the carbon sublattices introduces the finite band gap in graphene sandwiched between the oxide monolayers.

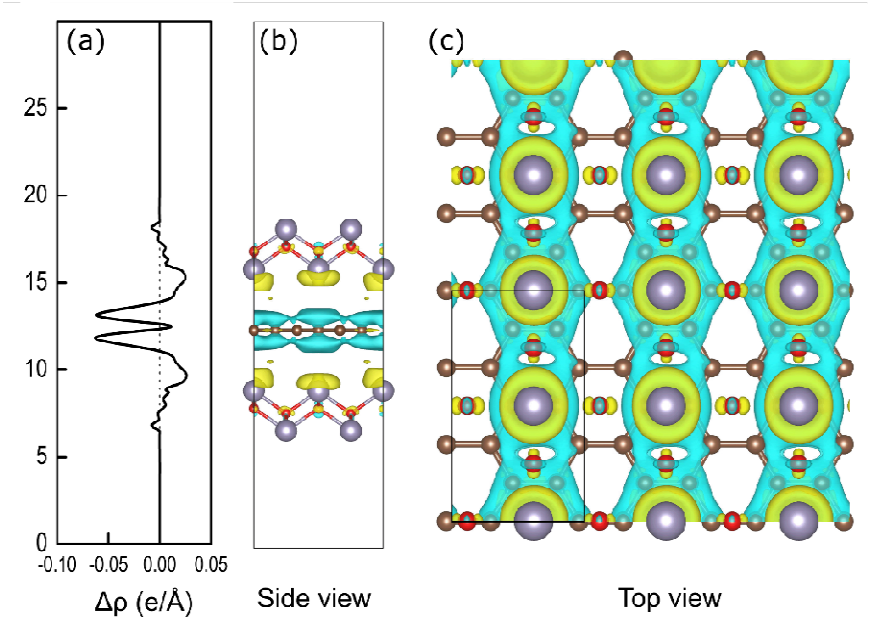

Figure S3. ABA-stacked SnO/graphene/SnO heterostructure: (a) The profile of the planar average charge density difference as a function of position along the z-direction. (b) side and (c) top views of the charge density difference with the isosurface value of 0.0014 e/Å ^{3}. The yellow and blue colors represent electron-rich and electron deficient regions, respectively. Color code: C: small brown sphere, Sn: large grey sphere and O: small red sphere.

S4. Comparison of results obtained using PBE-D2 and optB88-vdW functional forms

Note that both PBE-D2 and optB88-vdW level of theory provide similar results (Table S1). The band gap difference between the PBE-D2 and optB88-vdW functional forms comes out to be about 3~4 meV (Table S2). On the other hand, a larger gap is predicted for the HSE functional form, as expected.

Table S1 Total energy of SnO/graphene/SnO trilayer calculated using optB88-vdW and PBE-D2 functional forms.

Stacking Configuration	Relative Energy (eV)	
	PBE-D2	optB88-vdW
ABA	0	0
ABC	0.005	0.003
AAA	0.035	0.016

Table S2. Calculated band gaps of the ABA-stacked SnO/graphene/SnO tri-layer for the PBE-D2 optimized trilayer configuration.

Functional form	Band gap (eV)
PBE-D2	0.115 eV
optB88-vdW	0.111 eV
HSE06	0.240 eV

S5. Calculated band structures of SnO monolayer and SnO Bulk

The calculated band structure of a SnO monolayer is distinctly different from that of SnO bulk (Figure S4). A large direct band gap is predicted for SnO monolayer while a very small indirect band gap exists for SnO bulk [3, 4]. We also notice that the valence bands of SnO monolayer are much flatter that of bulk SnO.

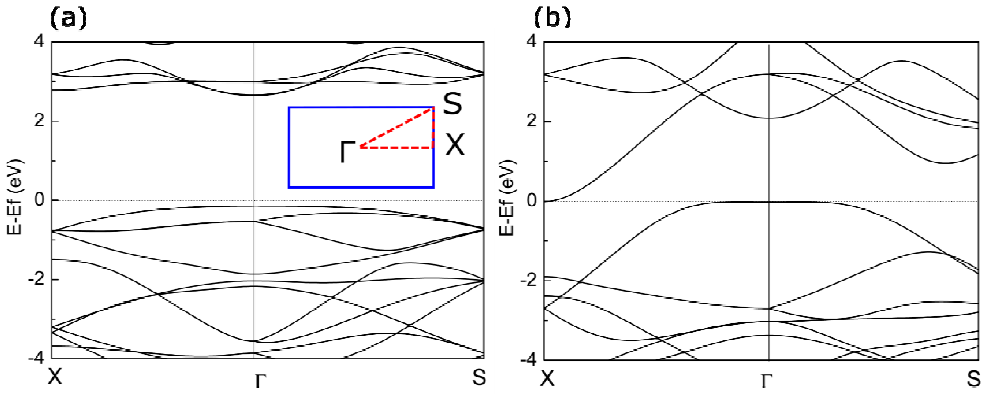

Figure S4: Calculated (PBE-D2) band structures of (a) SnO monolayer, and (b) SnO bulk.

S6. Multilayer heterostructures : ABAA- stacked SnO/graphene/SnO-bilayer and ABAAA-stacked SnO/graphene/SnO-trilayer heterostructures

As shown in Figure S5, top of the valence band associated with SnO layers has risen to the Fermi level with the increase of the substrate thickness. Consequently, the band gap is closed in graphene/oxide heterostructures with a thicker SnO substrate which will result in an Ohmic conductivity in the heterostructure.

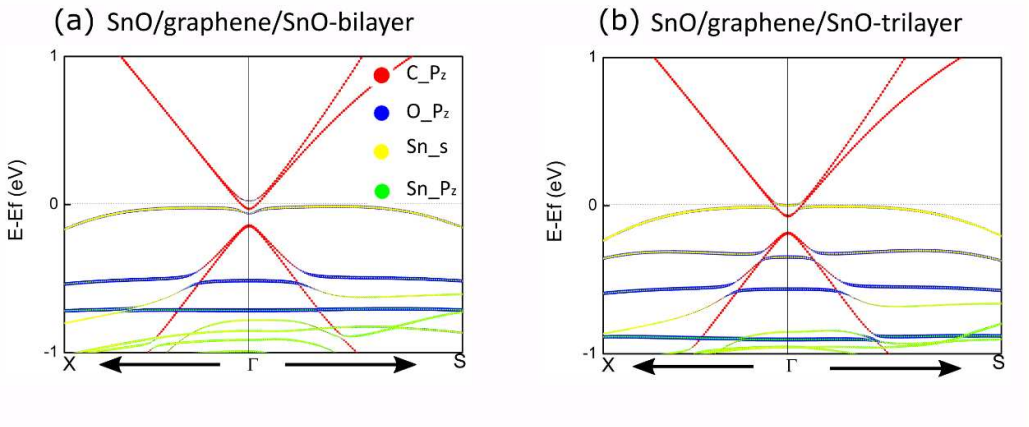

Figure S5: Calculated (PBE-D2) band structures of (a) ABAA SnO/graphene/SnO-bilayer and ABAAA SnO/graphene/SnO-trilayer heterostructures.

S7. Structure of the ABA and AAA stacked SnO/graphene/SnO trilayer

AAA.cif:

```
#======================================================================

# CRYSTAL DATA

#----------------------------------------------------------------------

data_VESTA_phase_1


_pd_phase_name                         'hetero                                '
_cell_length_a                         4.23948
_cell_length_b                         7.37038
_cell_length_c                         30.00000
_cell_angle_alpha                      90
_cell_angle_beta                       90
_cell_angle_gamma                      90
_symmetry_space_group_name_H-M         'P 1'
_symmetry_Int_Tables_number            1

loop_
_symmetry_equiv_pos_as_xyz
   'x, y, z'

loop_
   _atom_site_label
   _atom_site_occupancy
   _atom_site_fract_x
   _atom_site_fract_y
   _atom_site_fract_z
   _atom_site_adp_type
   _atom_site_B_iso_or_equiv
   _atom_site_type_symbol
   Sn1     1.0     0.618792     0.000190     0.298922     Biso    1.000000 Sn
   Sn2     1.0     0.119215     0.249696     0.222843     Biso    1.000000 Sn
   Sn3     1.0     0.618547     0.500202     0.298430     Biso    1.000000 Sn
   Sn4     1.0     0.119345     0.750700     0.222844     Biso    1.000000 Sn
   Sn5     1.0     0.617509     0.001034     0.529313     Biso    1.000000 Sn
   Sn6     1.0     0.116944     0.250309     0.605457     Biso    1.000000 Sn
   Sn7     1.0     0.617113     0.501053     0.529905     Biso    1.000000 Sn
   Sn8     1.0     0.116657     0.751763     0.605464     Biso    1.000000 Sn
```

O1	1.0	0.118180	0.000221	0.265403	Biso	1.000000 O
O2	1.0	0.618204	0.249957	0.256335	Biso	1.000000 O
O3	1.0	0.118216	0.500223	0.265025	Biso	1.000000 O
O4	1.0	0.618234	0.750466	0.256337	Biso	1.000000 O
O5	1.0	0.116606	0.001026	0.562811	Biso	1.000000 O
O6	1.0	0.616504	0.250591	0.571955	Biso	1.000000 O
O7	1.0	0.116604	0.501023	0.563381	Biso	1.000000 O
O8	1.0	0.616459	0.751488	0.571978	Biso	1.000000 O
C1	1.0	0.209002	0.500151	0.413824	Biso	1.000000 C
C2	1.0	0.544077	0.500176	0.413844	Biso	1.000000 C
C3	1.0	0.709984	0.666563	0.413851	Biso	1.000000 C
C4	1.0	0.043050	0.666555	0.413851	Biso	1.000000 C
C5	1.0	0.210017	0.166334	0.413930	Biso	1.000000 C
C6	1.0	0.543017	0.166366	0.413933	Biso	1.000000 C
C7	1.0	0.709978	0.333780	0.413886	Biso	1.000000 C
C8	1.0	0.043006	0.333752	0.413878	Biso	1.000000 C
C9	1.0	0.210026	0.833984	0.413899	Biso	1.000000 C
C10	1.0	0.543037	0.833982	0.413902	Biso	1.000000 C
C11	1.0	0.708993	0.000174	0.413920	Biso	1.000000 C
C12	1.0	0.044096	0.000162	0.413918	Biso	1.000000 C

ABA.cif:

```
#======================================================================

# CRYSTAL DATA

#----------------------------------------------------------------------

data_VESTA_phase_1


_pd_phase_name                         'hetero                                '
_cell_length_a                         4.23948
_cell_length_b                         7.37038
_cell_length_c                         30.00000
_cell_angle_alpha                      90
_cell_angle_beta                       90
_cell_angle_gamma                      90
_symmetry_space_group_name_H-M         'P 1'
_symmetry_Int_Tables_number            1
```

```
loop_
_symmetry_equiv_pos_as_xyz
   'x, y, z'

loop_
   _atom_site_label
   _atom_site_occupancy
   _atom_site_fract_x
   _atom_site_fract_y
   _atom_site_fract_z
   _atom_site_adp_type
   _atom_site_B_iso_or_equiv
   _atom_site_type_symbol
   Sn1    1.0    0.618792    0.000190    0.298922    Biso    1.000000 Sn
   Sn2    1.0    0.119215    0.249696    0.222843    Biso    1.000000 Sn
   Sn3    1.0    0.618547    0.500202    0.298430    Biso    1.000000 Sn
   Sn4    1.0    0.119345    0.750700    0.222844    Biso    1.000000 Sn
   Sn5    1.0    0.617509    0.001034    0.529313    Biso    1.000000 Sn
   Sn6    1.0    0.116944    0.250309    0.605457    Biso    1.000000 Sn
   Sn7    1.0    0.617113    0.501053    0.529905    Biso    1.000000 Sn
   Sn8    1.0    0.116657    0.751763    0.605464    Biso    1.000000 Sn
   O1     1.0    0.118180    0.000221    0.265403    Biso    1.000000 O
   O2     1.0    0.618204    0.249957    0.256335    Biso    1.000000 O
   O3     1.0    0.118216    0.500223    0.265025    Biso    1.000000 O
   O4     1.0    0.618234    0.750466    0.256337    Biso    1.000000 O
   O5     1.0    0.116606    0.001026    0.562811    Biso    1.000000 O
   O6     1.0    0.616504    0.250591    0.571955    Biso    1.000000 O
   O7     1.0    0.116604    0.501023    0.563381    Biso    1.000000 O
   O8     1.0    0.616459    0.751488    0.571978    Biso    1.000000 O
   C1     1.0    0.959002    0.000151    0.413824    Biso    1.000000 C
   C2     1.0    0.294077    0.000176    0.413844    Biso    1.000000 C
   C3     1.0    0.459984    0.166563    0.413851    Biso    1.000000 C
   C4     1.0    0.793050    0.166555    0.413851    Biso    1.000000 C
   C5     1.0    0.960017    0.666334    0.413930    Biso    1.000000 C
   C6     1.0    0.293017    0.666366    0.413933    Biso    1.000000 C
   C7     1.0    0.459978    0.833780    0.413886    Biso    1.000000 C
   C8     1.0    0.793006    0.833752    0.413878    Biso    1.000000 C
   C9     1.0    0.960026    0.333984    0.413899    Biso    1.000000 C
   C10    1.0    0.293037    0.333982    0.413902    Biso    1.000000 C
   C11    1.0    0.458993    0.500174    0.413920    Biso    1.000000 C
   C12    1.0    0.794096    0.500162    0.413918    Biso    1.000000 C
```

References

1. Suzuki, A., M. Tanabe, and S. Fujita, *Electronic Band Structure of Graphene Based on the Rectangular 4-Atom Unit Cell.* Journal of Modern Physics, 2017. **8**(04): p. 607.
2. Dedkov, Y. and E. Voloshina, *Graphene growth and properties on metal substrates.* Journal of Physics: Condensed Matter, 2015. **27**(30): p. 303002.
3. Zhou, W. and N. Umezawa, *Band gap engineering of bulk and nanosheet SnO: an insight into the interlayer Sn-Sn lone pair interactions.* Phys Chem Chem Phys, 2015. **17**(27): p. 17816-20.
4. Du, J., et al., *Electronic characteristics of p-type transparent SnO monolayer with high carrier mobility.* Applied Surface Science, 2017. **401**: p. 114-119.